PLANETAS EXTRASOLARES

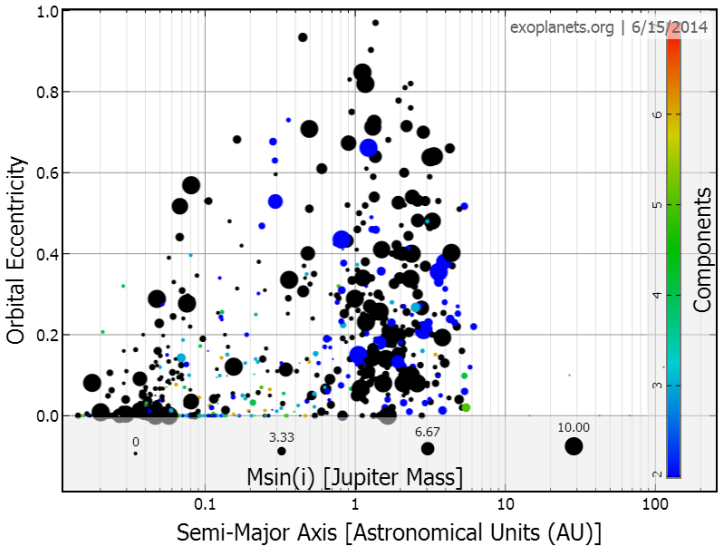

Curso Planetología 2014

Tabaré Gallardo

exoplanets.org

Exoplanets Data Explorer | Methodology and FAQ | Exoplanets Links | California Planet Survey

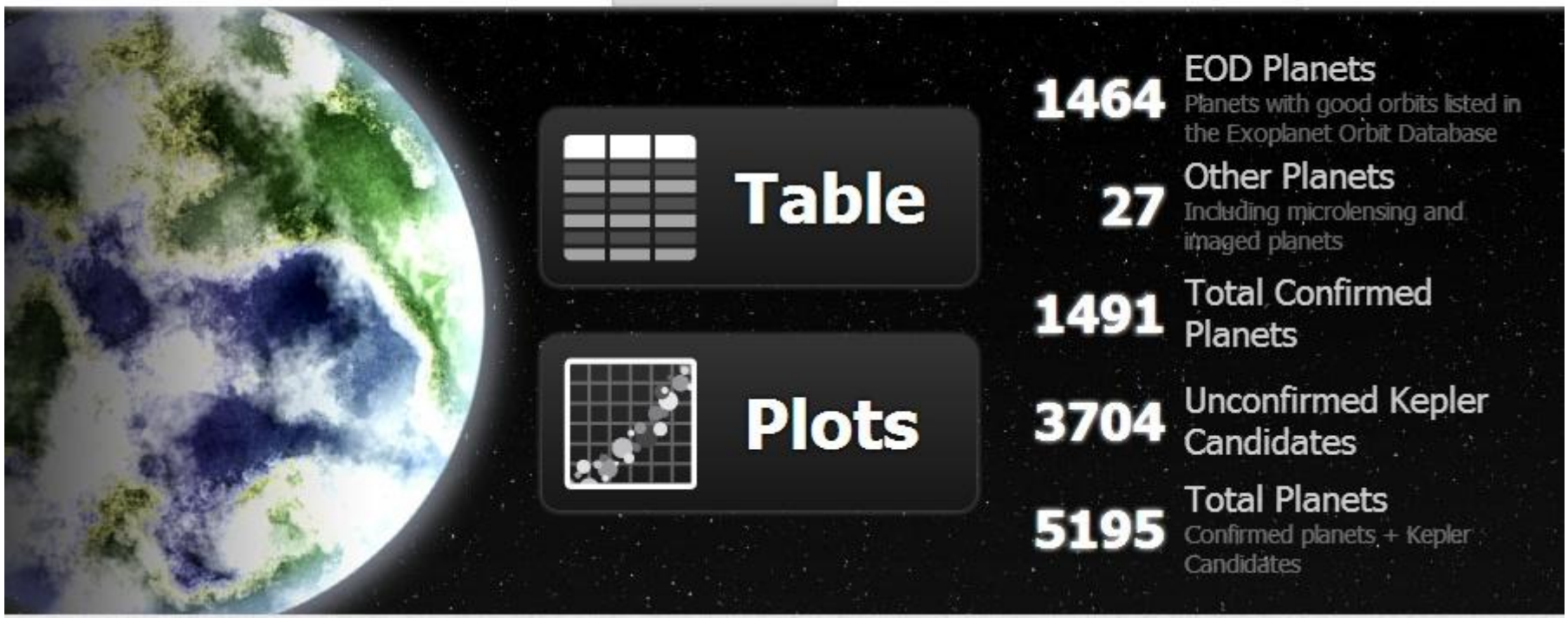

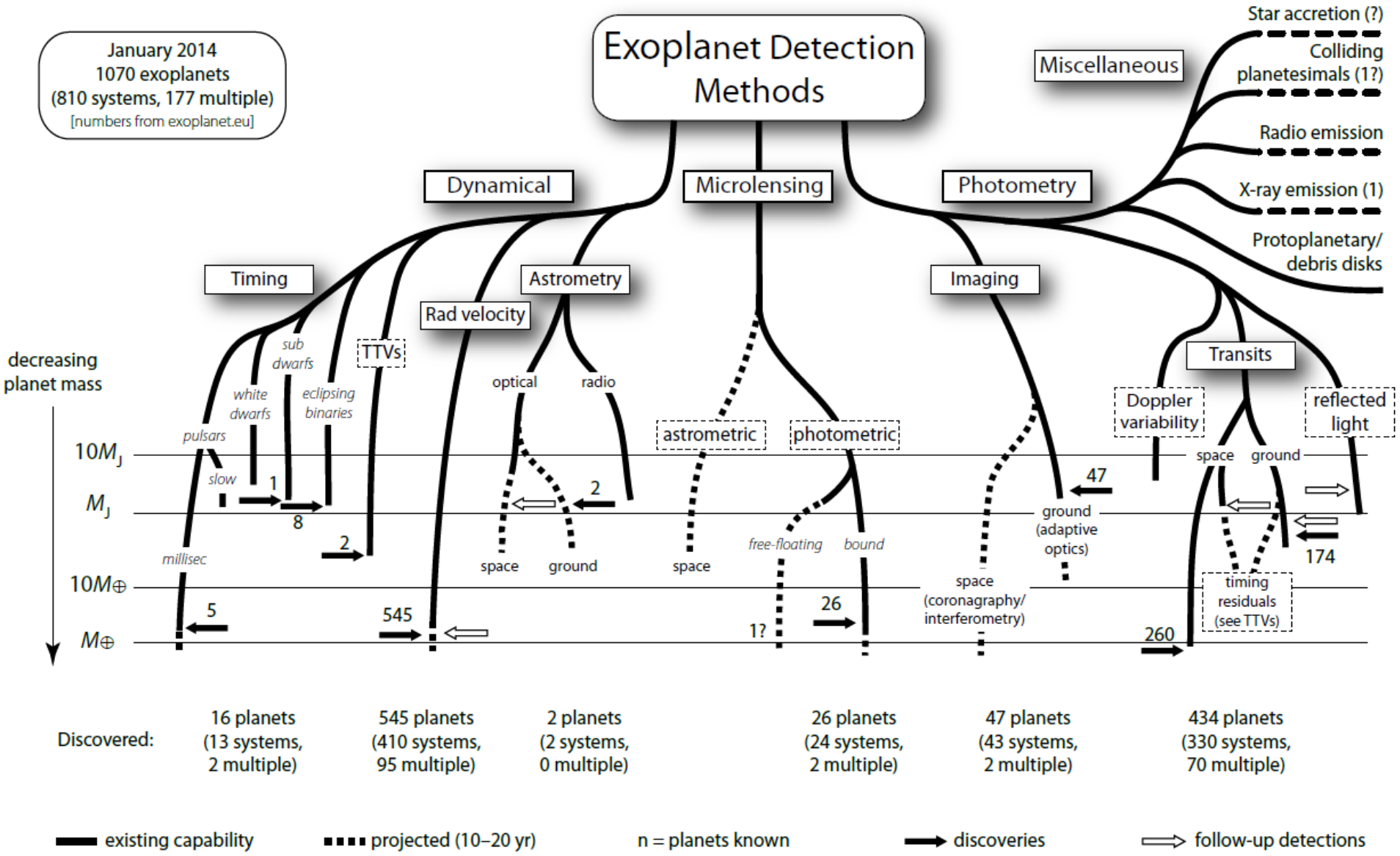

Figure 1.1: Detection methods for exoplanets. The lower limits of the lines indicate the detectable masses that are in principle within reach of present measurements (solid lines), and those that might be expected within the next 10–20 years (dashed). The (logarithmic) mass scale is shown at left. The miscellaneous signatures to the upper right are less well quantified in mass terms. Solid arrows indicate detections according to approximate mass. Open arrows indicate that relevant measurements of previously-detected systems have been made. The figure takes no account of the numbers of planets that may ultimately be detectable by each method. Adapted from Perryman (2000, Figure 1), with permission from the Institute of Physics Publishing Ltd.

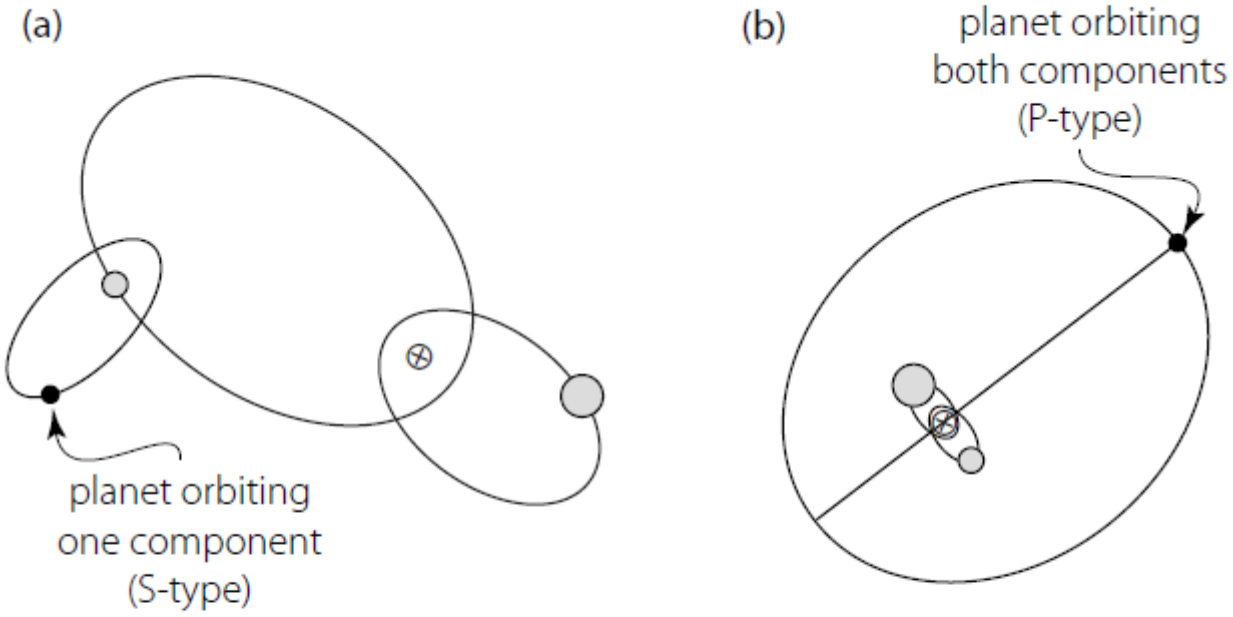

Figure 2.44: Schematic of a planet in a binary star system (⊗ indicates the stellar centre of mass): (a) the planet orbits one component of the stellar binary; (b) the planet is in a circumbinary orbit about both stellar components.

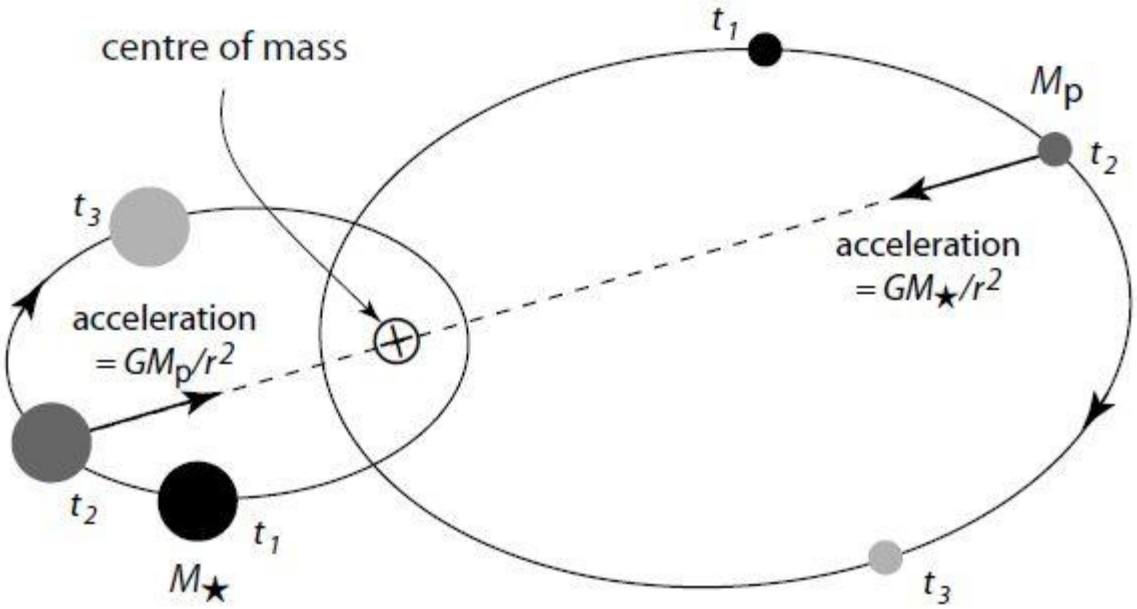

Figure 2.3: Two orbiting bodies, shown at times t_1, t_2, t_3, move about their common barycentre. Both bodies follow orbits having the same shape and period, but of different sizes and with ω differing by $180°$.

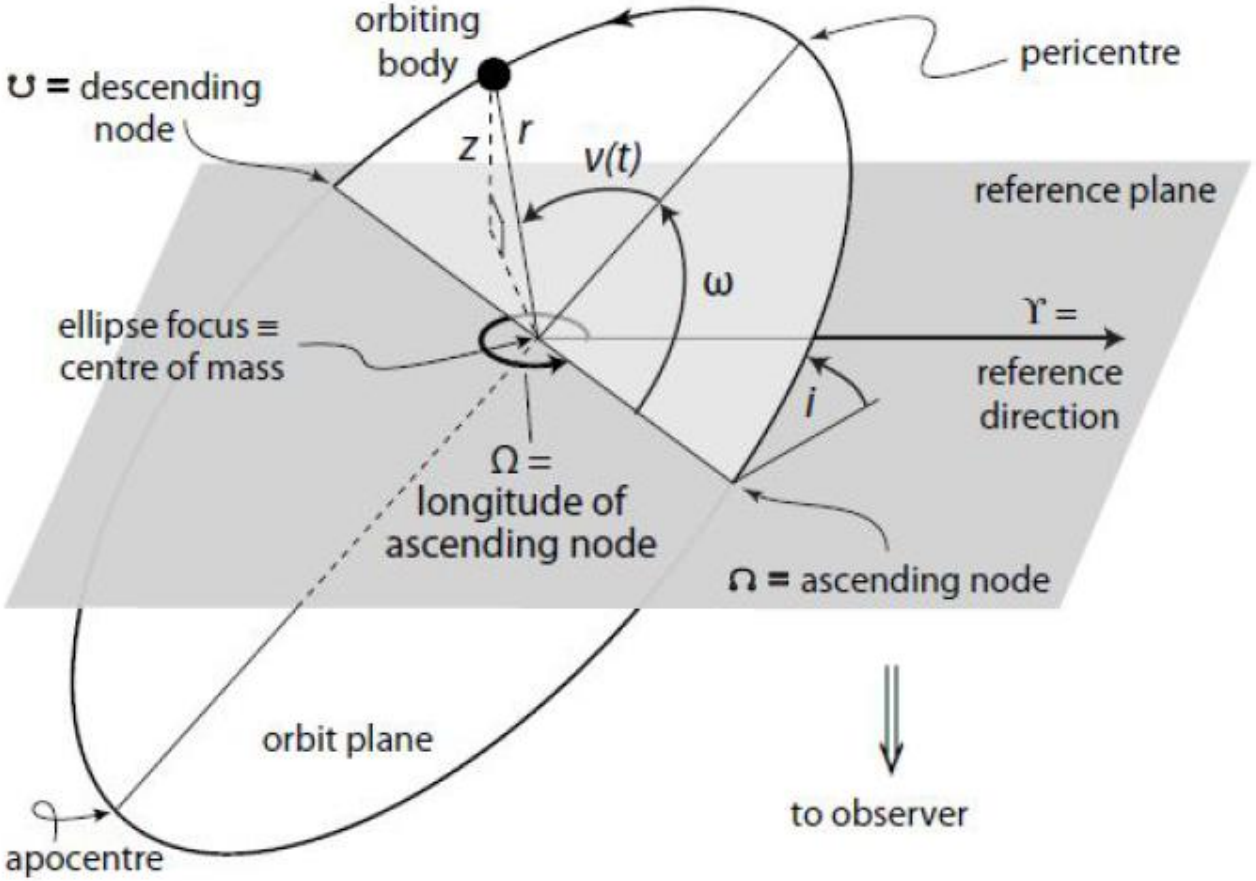

Figure 2.2: An elliptical orbit in three dimensions. The reference plane is tangent to the celestial sphere. i is the inclination of the orbit plane. The nodes are the points where the orbit and reference planes intersect. Ω defines the longitude of the ascending node, measured in the reference plane. ω is the fixed angle defining the object's argument of pericentre relative to the ascending node. The true anomaly, $\nu(t)$, is the time-dependent angle characterising the object's position along the orbit.

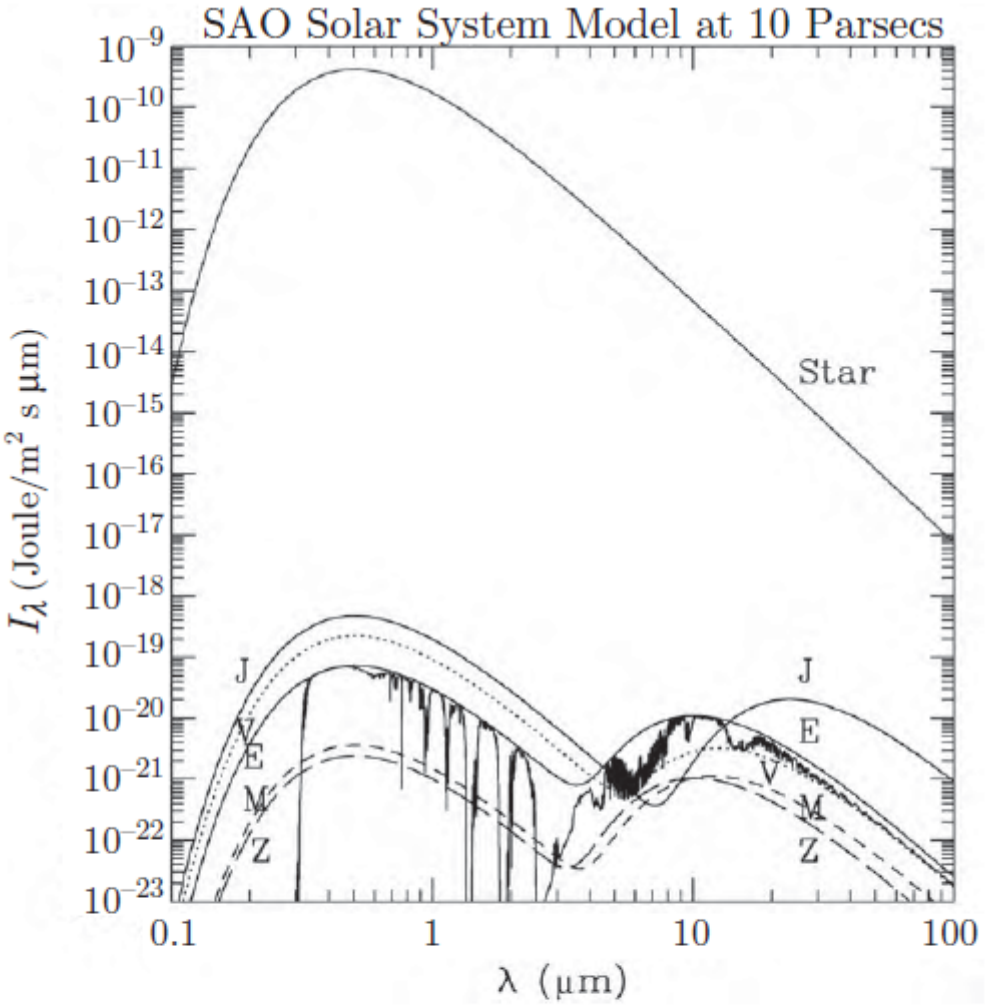

Figure 14.5 Spectral energy distribution of the Sun, Jupiter, Venus, Earth, Mars and the zodiacal cloud. The bodies are approximated by blackbodies of uniform albedo, with an additional curve showing Earth's atmospheric absorption features. (Adapted from Des Marais et al. 2002)

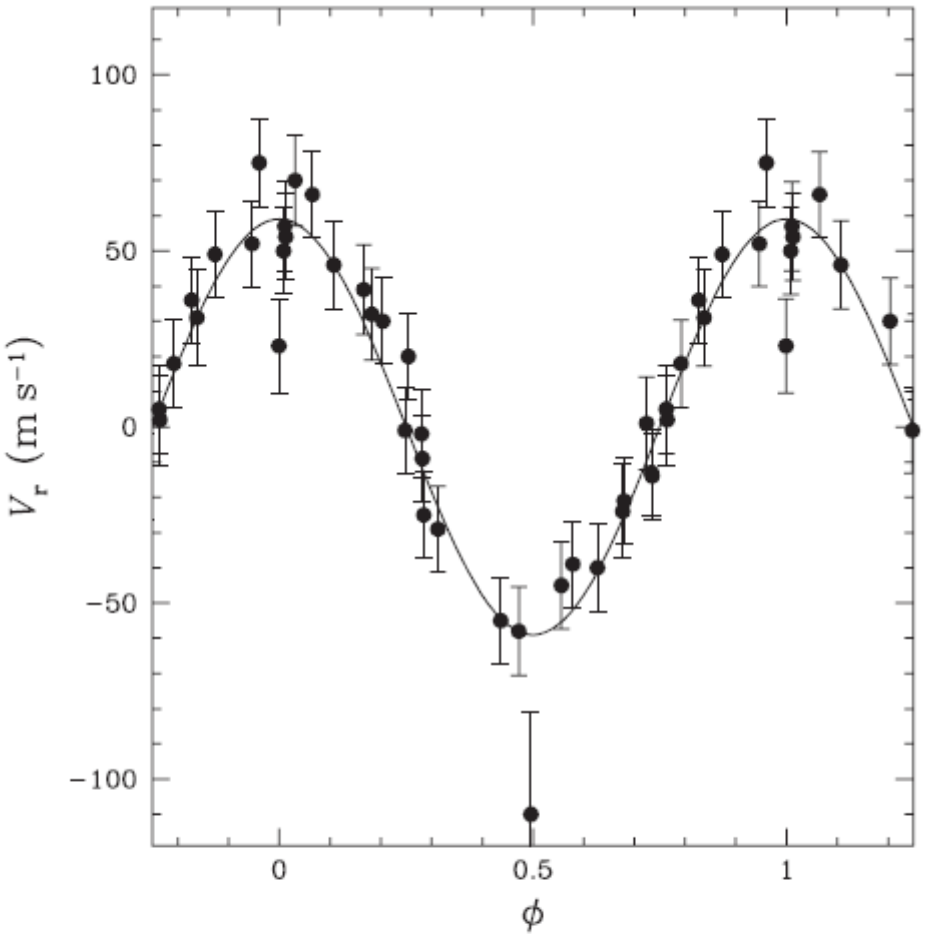

Figure 14.9 Radial velocity measurements of the star 51 Pegasi (*points with error bars*) as a function of phase of the orbital fit (*solid line*). These data were used to discover the first planet found around a main sequence star other than the Sun. One and a half cycles are shown for clarity. (Adapted from Mayor and Queloz 1995; courtesy Didier Queloz)

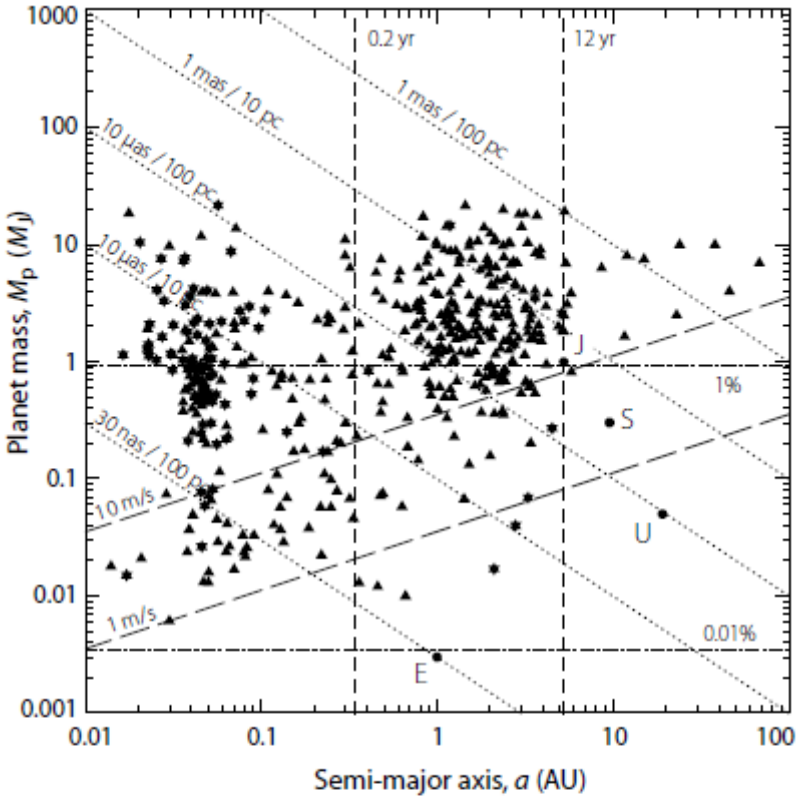

Figure 2.18: Detection domains based on orbital motion. Lines from top left to bottom right show astrometric signatures of 1 mas and 10 μas at distances of 10 and 100 pc (Equation 3.1, assuming $M_\star = M_\odot$). Short- and long-periods cannot be detected by planned space missions: vertical lines show limits at $P = 0.2$ and 12 yr. Lines from top right to bottom left show radial velocity semi-amplitudes of $K = 10$ and $K = 1\ \mathrm{m\,s^{-1}}$. Horizontal lines are transit thresholds of 1% and 0.01%, corresponding to $\sim 1 R_J$ and $\sim 1 R_\oplus$ respectively. Positions of E(arth), (J)upiter, (S)aturn and (U)ranus are shown, as are planets discovered from radial velocity ($M_p \sin i$, ▲) and transit photometry (★). Data are from `exoplanet.eu`, *2010–11–01.*

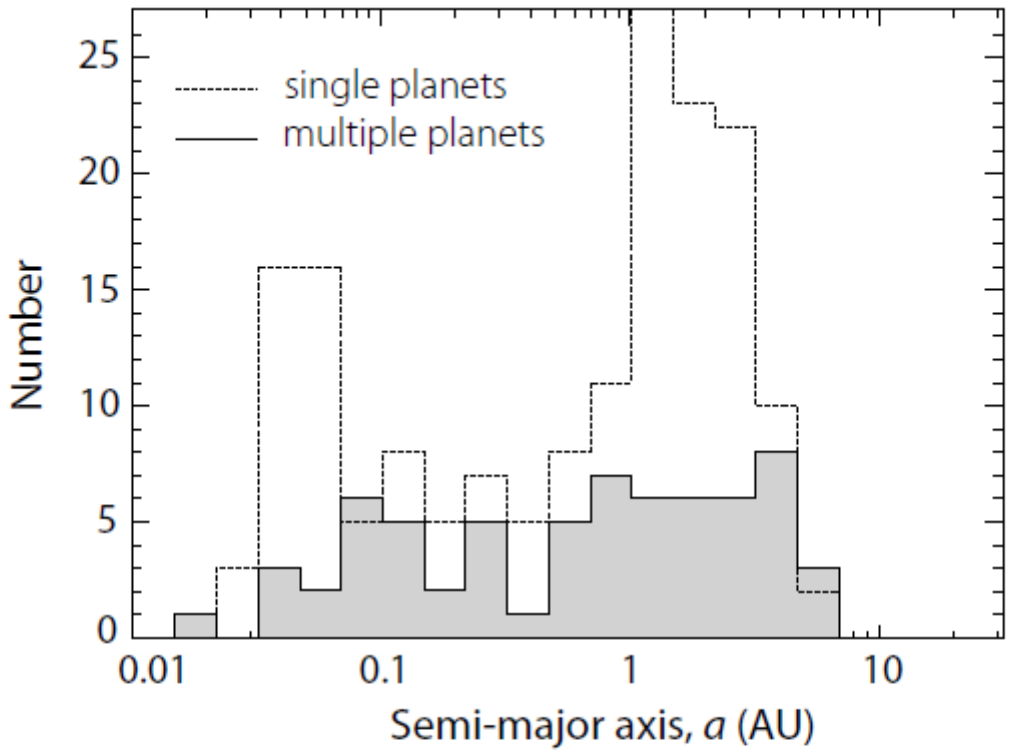

Figure 2.30: Distribution of semi-major axes for multiple planet systems (solid) and apparently single systems (dashed). The pile-up of hot Jupiters, and the jump in abundance beyond 1 AU seen in the single planet systems are not evident in the multiple planet systems. From Wright et al. (2009b, Figure 9), reproduced by permission of the AAS.

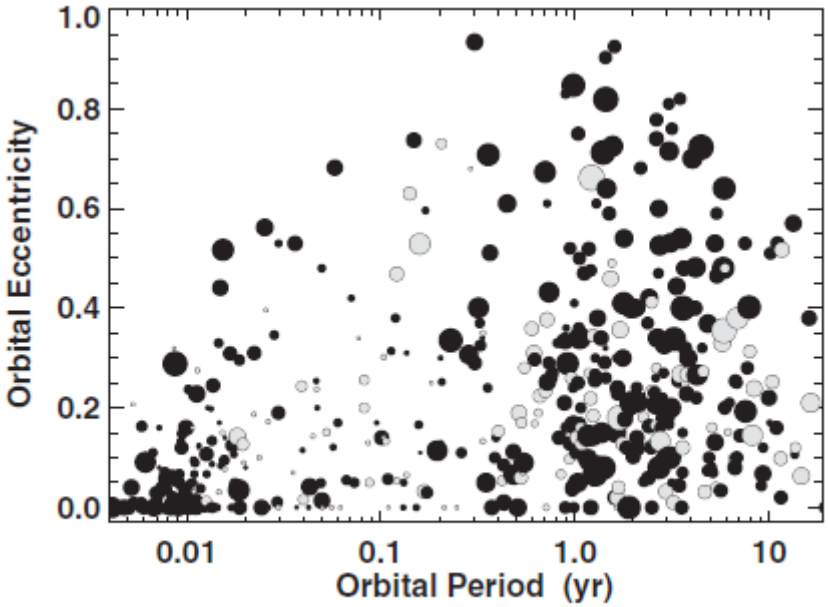

Figure 14.22 The eccentricities of the more than 600 exoplanets that have well-determined orbits (as of mid-2012) are plotted against orbital period. The *dot size* is proportional to $(M_p \sin i)^{1/3}$, and the *gray points* represent planets in systems known to possess more than one planet. Whereas the eccentricities of almost all of those planets with periods of less than a week are quite small (consistent with 0), presumably as a result of tidal damping, the eccentricities of planets with longer orbital periods are generally much larger than those of the giant planets within our Solar System. The vast majority of these planets were discovered by radial velocity, although the majority of those with periods of less than one week were first detected by ground-based transit surveys and *Kepler* discovered more than a dozen of the planets with low eccentricities and periods less than a few months. (Courtesy Geoff Marcy)

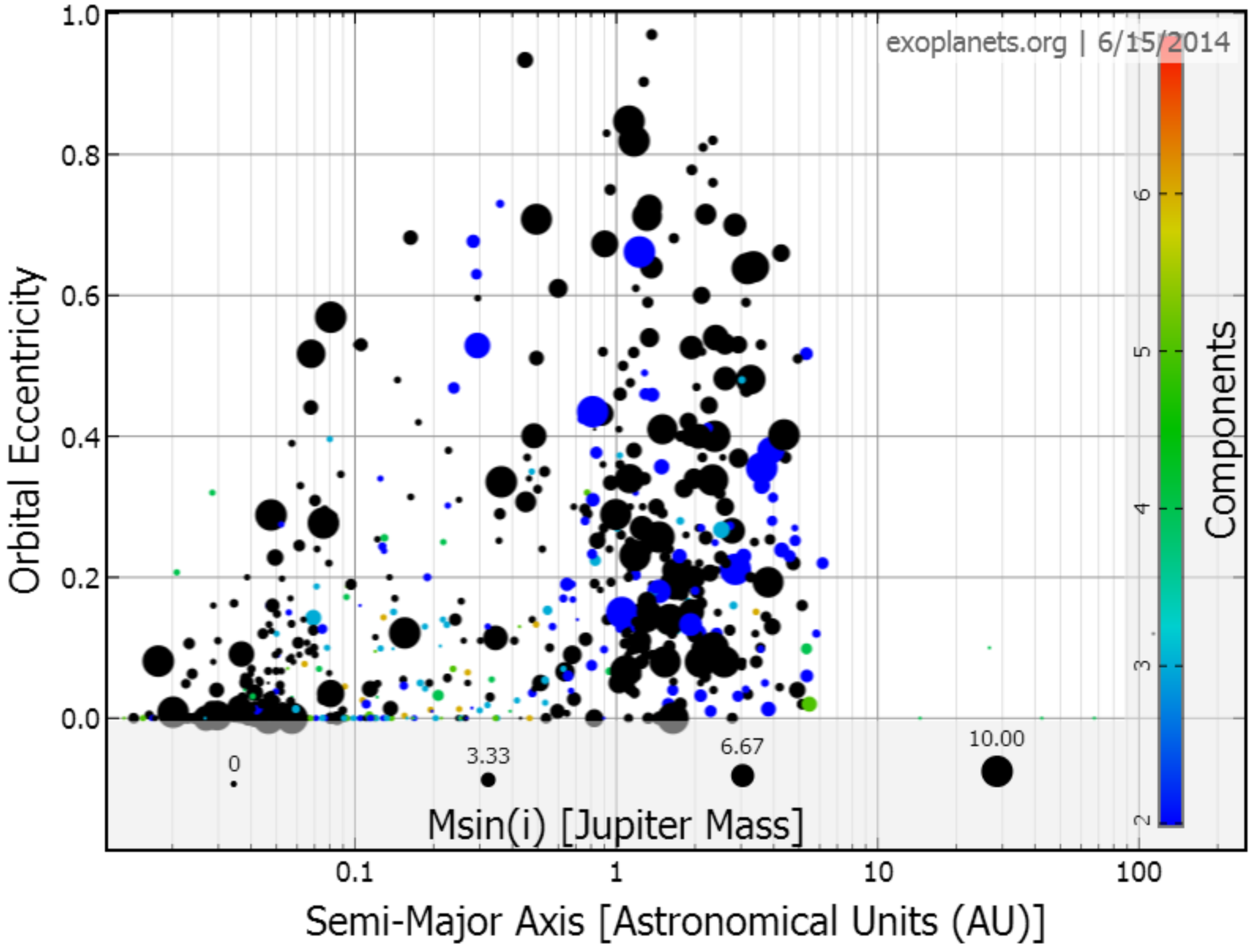
exoplanets.org | 6/15/2014
Orbital Eccentricity
1.0
0.8
0.6
0.4
0.2
0.0
Components
2
3
4
5
6
0
3.33
6.67
10.00
Msin(i) [Jupiter Mass]
0.1
1
10
100
Semi-Major Axis [Astronomical Units (AU)]

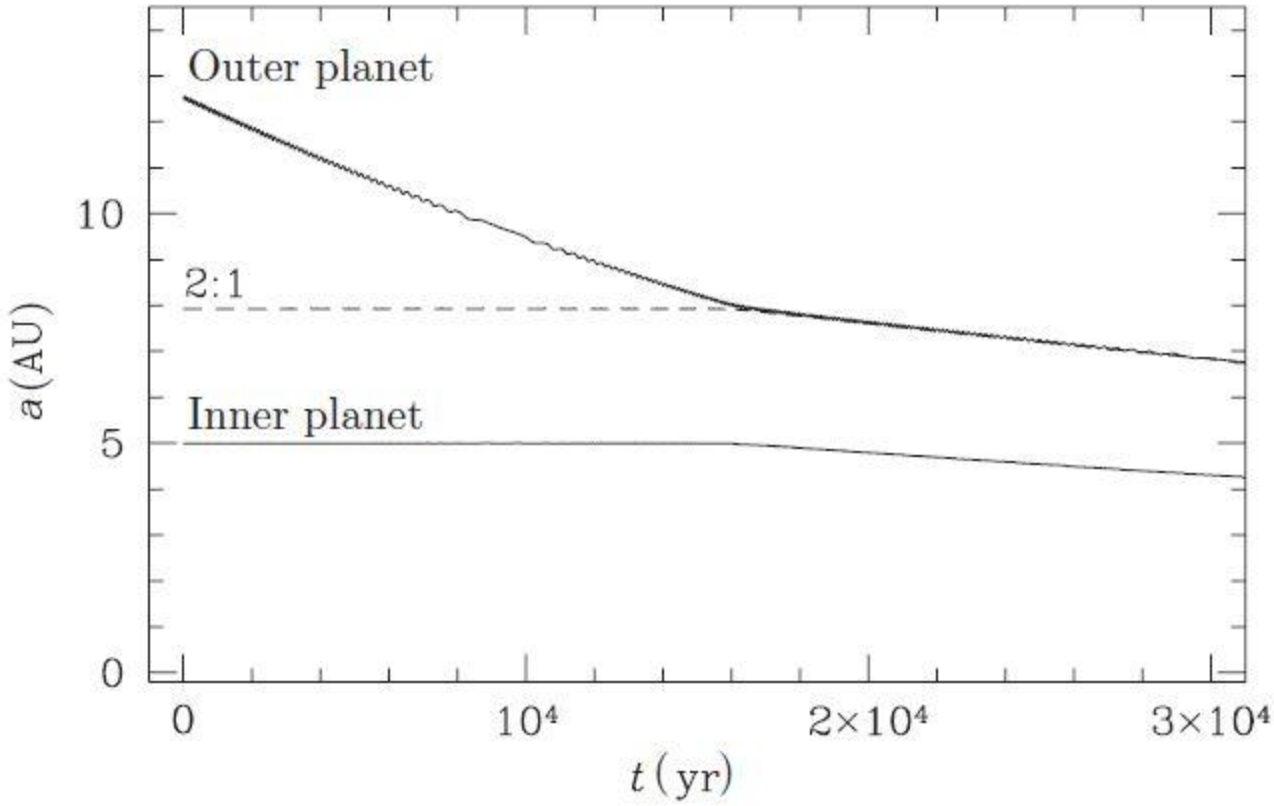

Fig. 7.5. Numerical example of resonant capture in a coplanar system of two initially well-separated Jupiter mass planets. For illustrative purposes the outer planet is subjected to a fictitious drag force which results in steady decay of its semi-major axis. The inner planet is almost unperturbed until the planets encounter their mutual 2:1 mean-motion resonance, at which point capture occurs and the two planets move inward in lockstep.

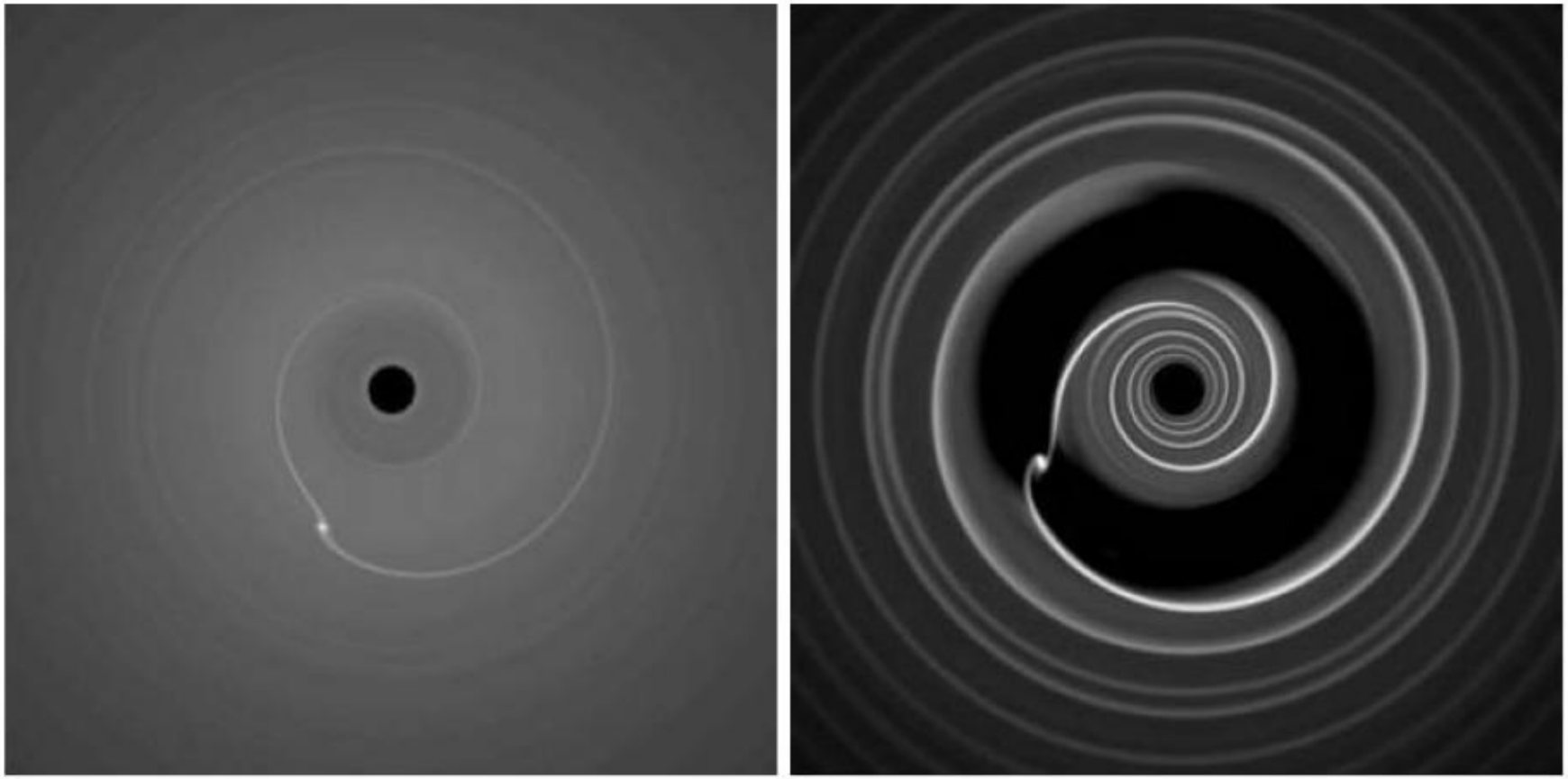

Fig. 7.1. Two-dimensional hydrodynamic simulations depicting the interaction between a planet and a viscous protoplanetary disk in (left panel) the Type 1 regime appropriate to low-mass planets and (right panel) the Type 2 regime relevant to giant planets. In both cases angular momentum exchange is the result of gravitational interaction with spiral waves set up within the disk as a consequence of the planetary perturbation. In the Type 1 regime the interaction is weak enough that the local surface density is approximately unperturbed, while in the Type 2 regime a strong interaction repels gas from the vicinity of the planet producing an annular gap.

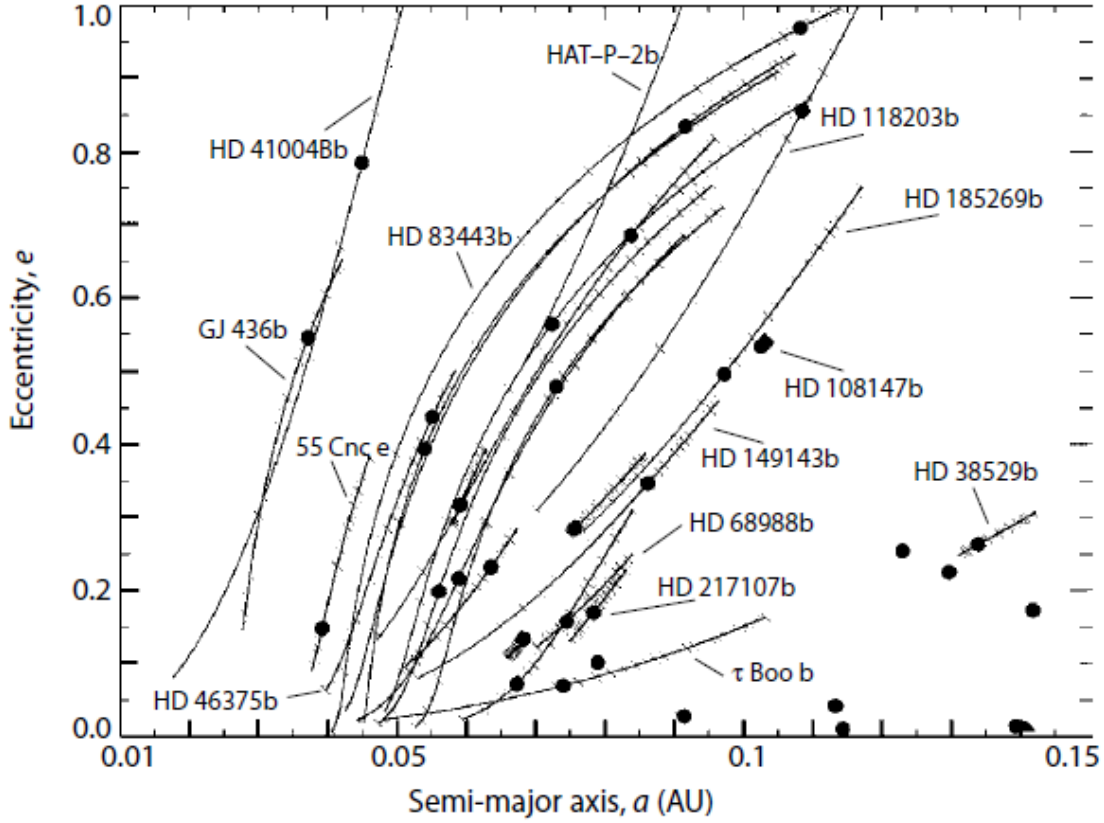

Figure 10.19: Tidal evolution of e and a for the sample of known close-in extrasolar planets using best-fit values of $Q_p = 10^{6.5}$ *and* $Q_\star = 10^{5.5}$ *obtained from a match between predicted initial eccentricities, and the distribution of eccentricities of more distant orbiting planets. Solid curves represent the trajectories of orbital evolution from current orbits (lower left end of each curve) backward in time (toward the upper right). Tick marks are spaced every 500 Myr to indicate the rate of tidal evolution. Tidal integrations were performed for 15 Gyr for all planets, but the filled circles indicate the initial values of orbital elements at the beginning of each planet's life. From Jackson et al. (2008b, Figure 7), reproduced by permission of the AAS.*

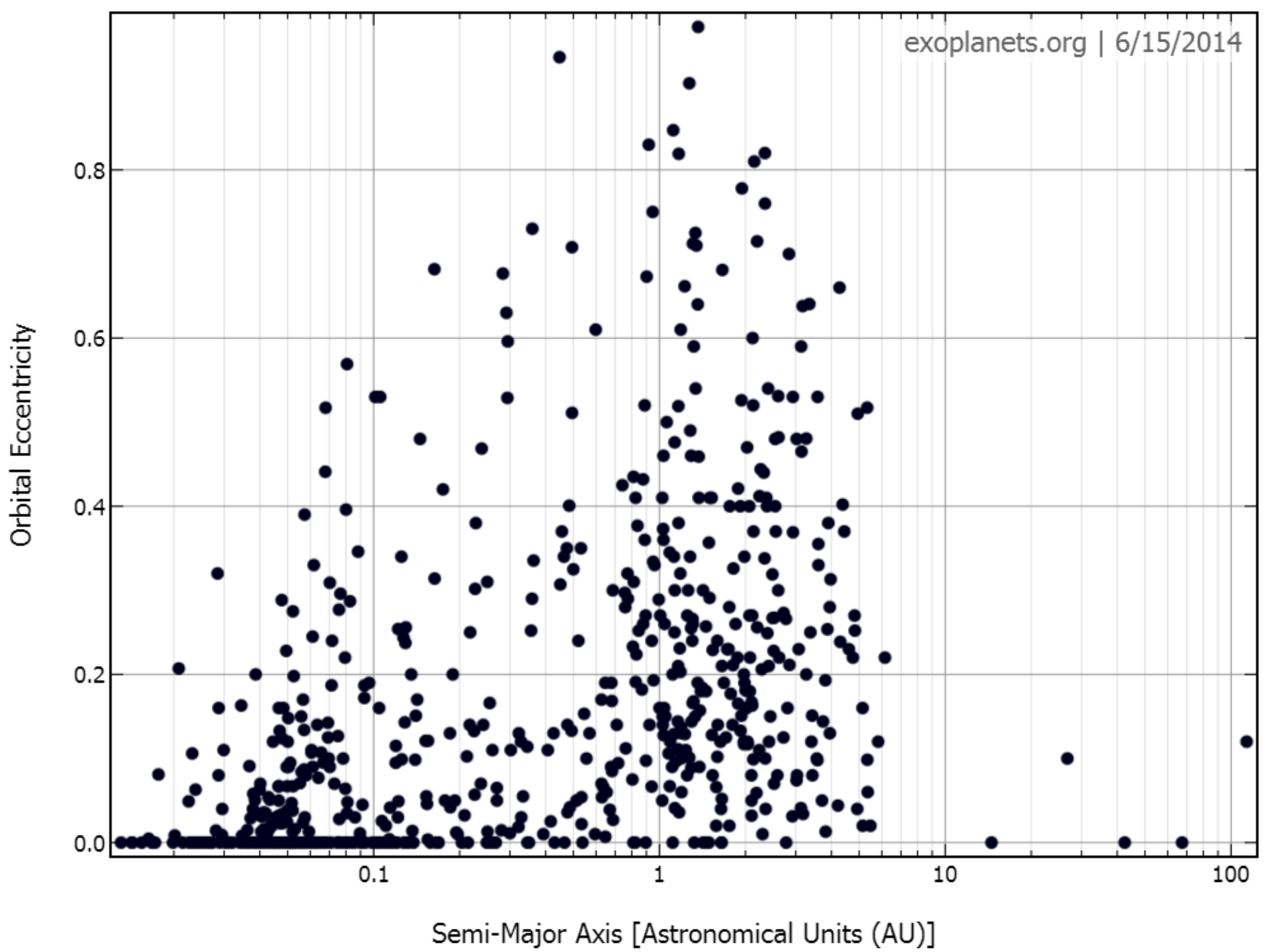
exoplanets.org | 6/15/2014
Orbital Eccentricity
0.0
0.2
0.4
0.6
0.8
0.1
1
10
100
Semi-Major Axis [Astronomical Units (AU)]

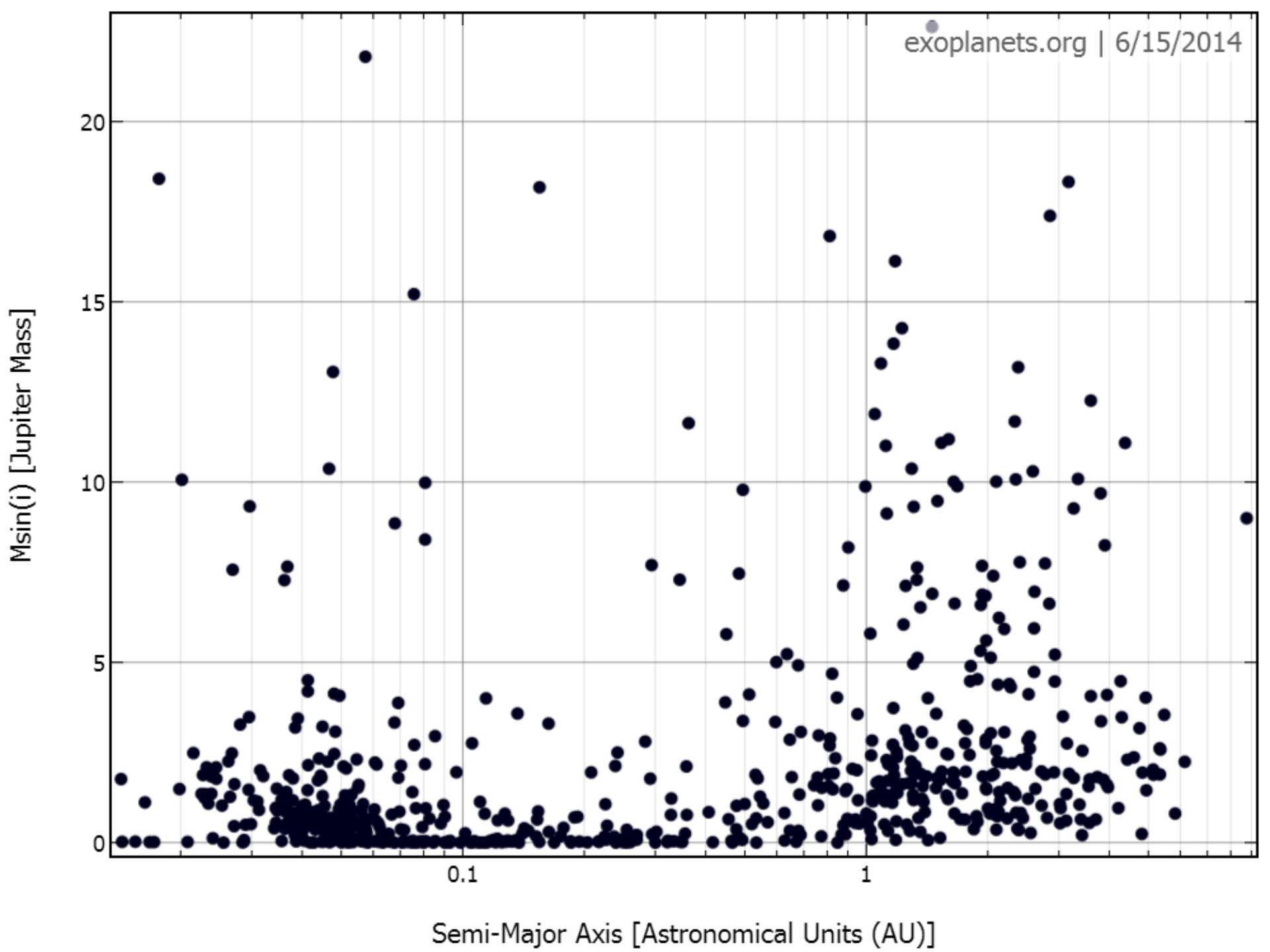
exoplanets.org | 6/15/2014
Msin(i) [Jupiter Mass]
20
15
10
5
0
0.1
1
Semi-Major Axis [Astronomical Units (AU)]

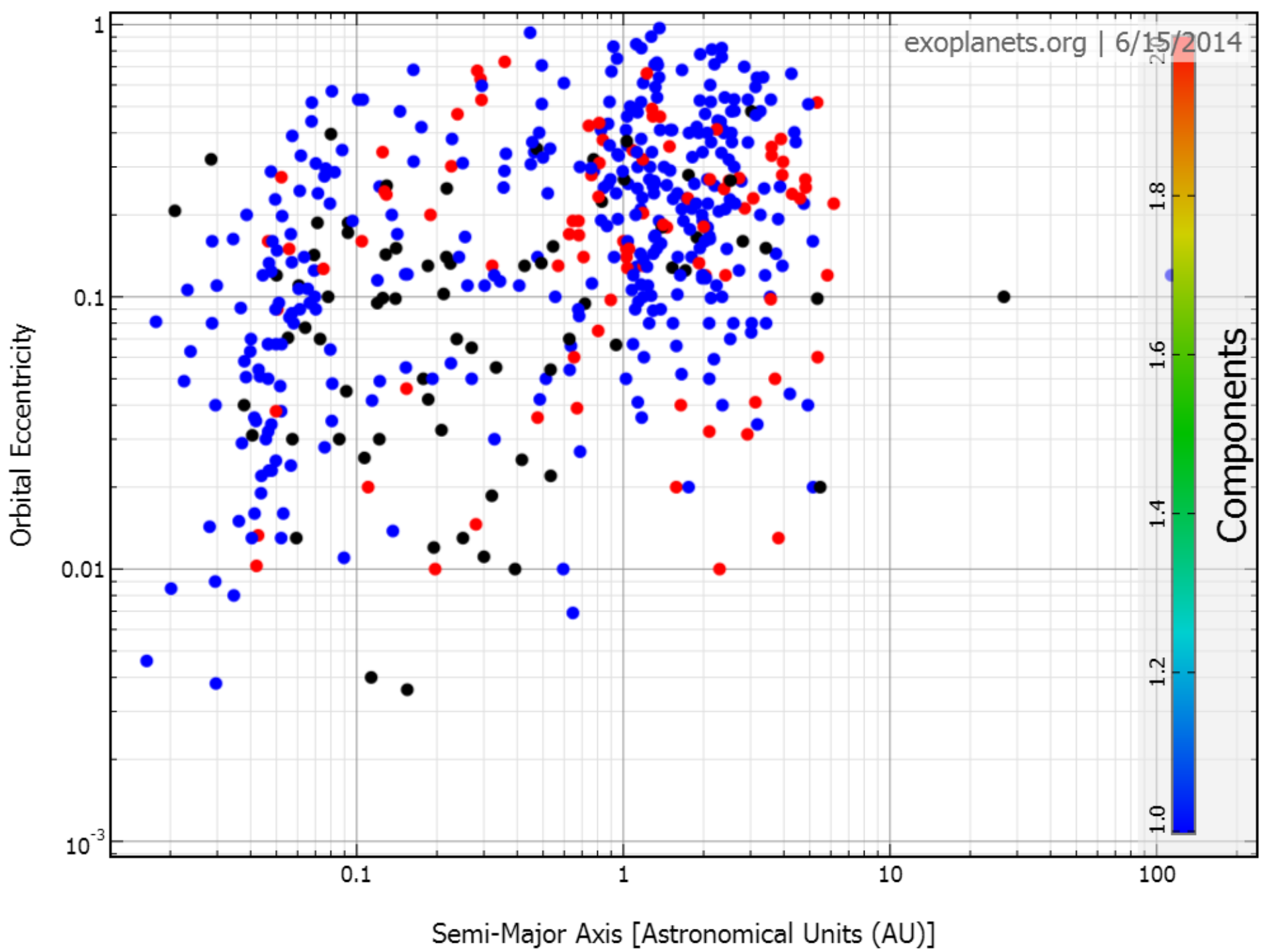
exoplanets.org | 6/15/2014
Orbital Eccentricity
1
0.1
0.01
10^{-3}
0.1
1
10
100
Semi-Major Axis [Astronomical Units (AU)]
Components
1.0
1.2
1.4
1.6
1.8

SUPER-EARTHS RISING

Ground-based telescopes have detected around 650 planets from the wobble of their parent star. A new class of planet — between the size of Earth and Neptune — has emerged precisely where modellers have said planets shouldn't exist.

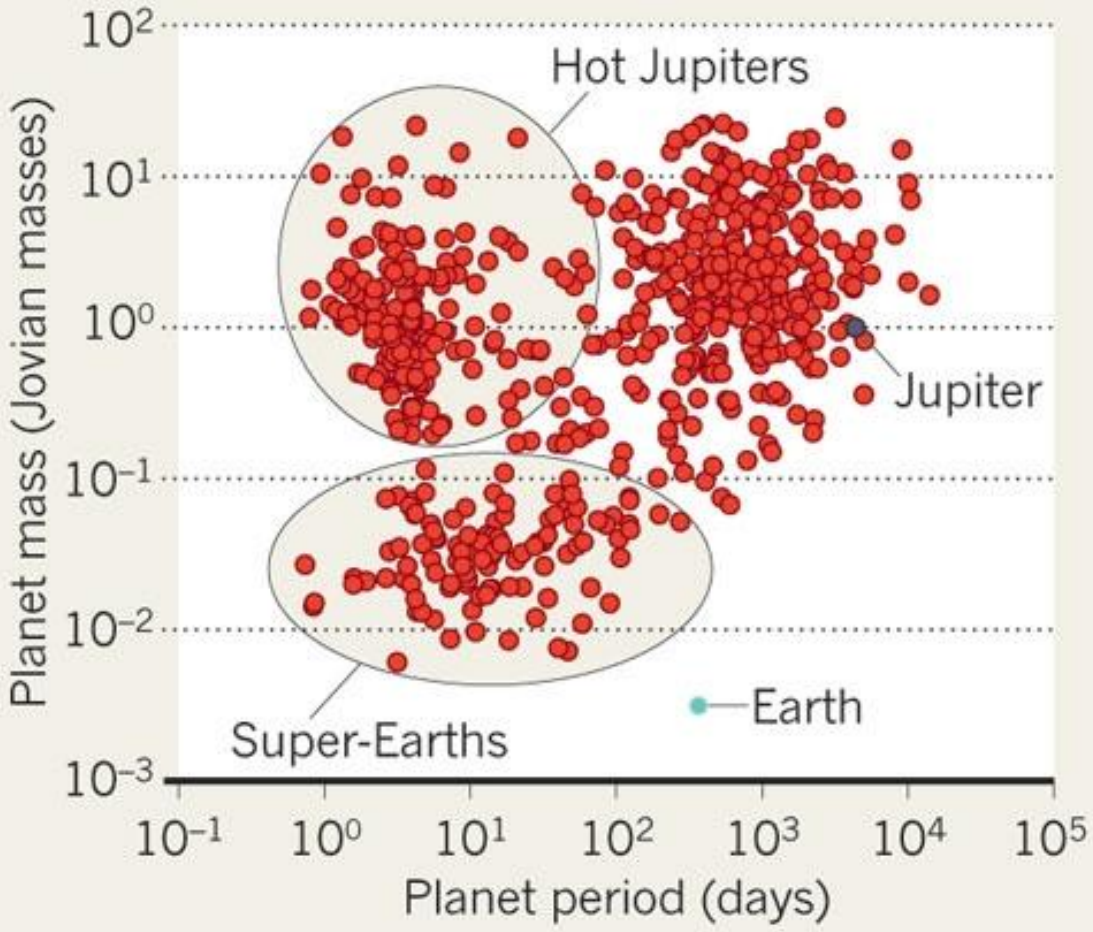

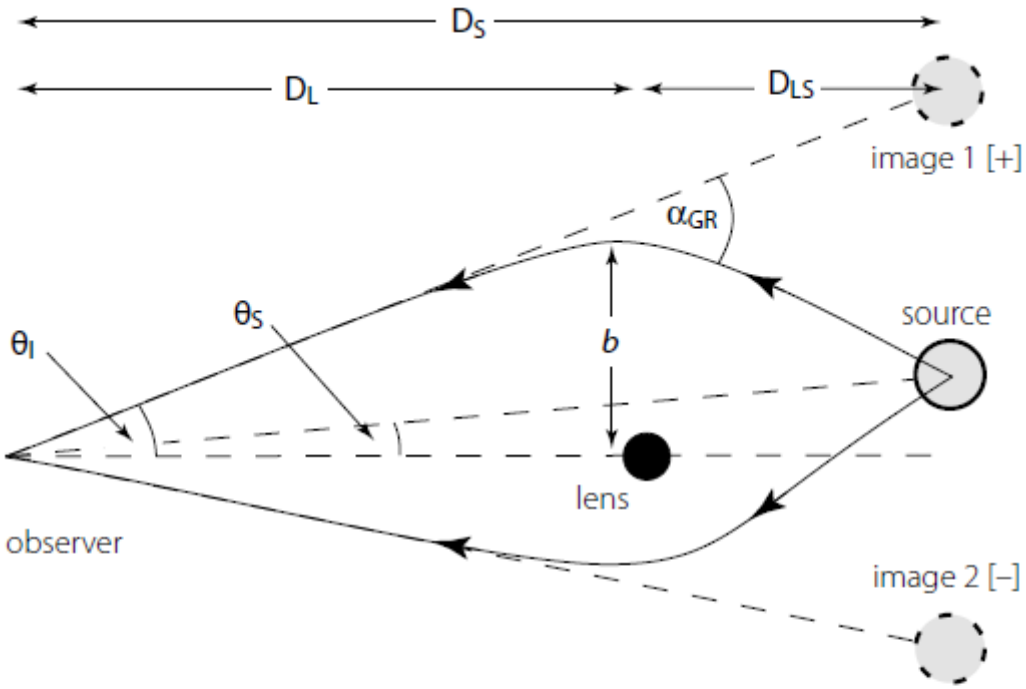

Figure 5.1: Lensing schematic for a point mass lens M_L at distance D_L, offset by the small angle θ_S from the direct line from observer to source. A light ray from the source, passing the lens at distance b, is deflected by an angle α_{GR}. An observer sees one image of the source displaced to angular position $\theta_I = b/D_L$ on the same side as the source, and a second image on the other.

The MACHO Project: Microlensing Results from 5.7 Years of LMC Observations

The MACHO collaboration: C. Alcock, R.A. Allsman, D.R. Alves, T.S. Axelrod, A.C. Becker, D.P. Bennett, K.H. Cook, N. Dalal, A.J. Drake, K.C. Freeman, M. Geha, K. Griest, M.J. Lehner, S.L. Marshall, D. Minniti, C.A. Nelson, B.A. Peterson, P. Popowski, M.R. Pratt, P.J. Quinn, C.W. Stubbs, W. Sutherland, A.B. Tomaney, T. Vandehei, D. Welch

(Submitted on 15 Jan 2000)

We report on our search for microlensing towards the Large Magellanic Cloud (LMC). Analysis of 5.7 years of photometry on 11.9 million stars in the LMC reveals 13 - 17 microlensing events. This is significantly more than the $\sim$ 2 to 4 events expected from lensing by known stellar populations. The timescales ($\that$) of the events range from 34 to 230 days. We estimate the microlensing optical depth towards the LMC from events with $2 < \that < 400$ days to be 1.2 ^{+0.4}_

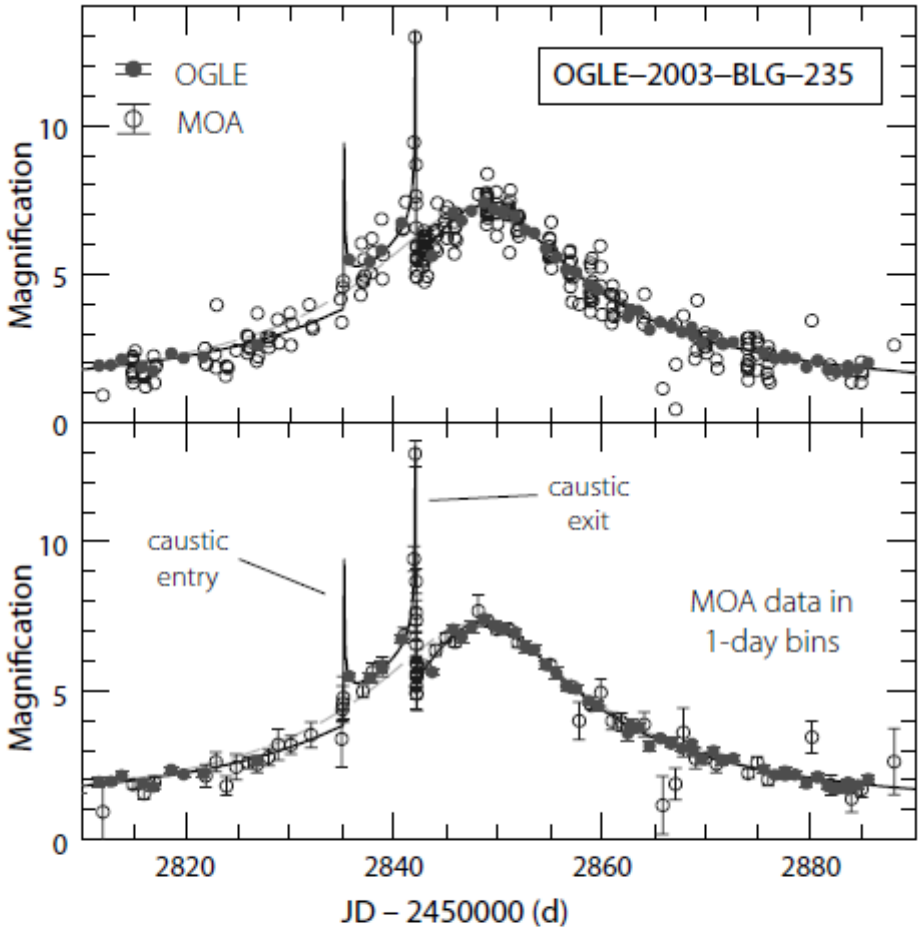

Figure 5.14: The first microlensing planet system, OGLE–2003–BLG–235, with data from OGLE and MOA over a period of about 80 days during 2003. The bottom panel shows binned data. Caustic crossings (entry and exit) occur on days 2835 and 2842. The binary and single lens fits are shown by the solid and fainter (lower) lines respectively. From Bond et al. (2004, Figure 1), reproduced by permission of the AAS.

Free-Floating Planets May be More Common Than Stars

This artist's conception illustrates a Jupiter-like planet alone in the dark of space, floating freely without a parent star. Astronomers recently uncovered evidence for 10 such lone worlds, thought to have been "booted," or ejected, from developing solar systems. Image credit: NASA/JPL-Caltech › Full image and caption | › See animation

May 18, 2011

PASADENA, Calif. -- Astronomers, including a NASA-funded team member, have discovered a new class of Jupiter-sized planets floating alone in the dark of space, away from the light of a star. The team believes these lone worlds were probably ejected from developing planetary systems.

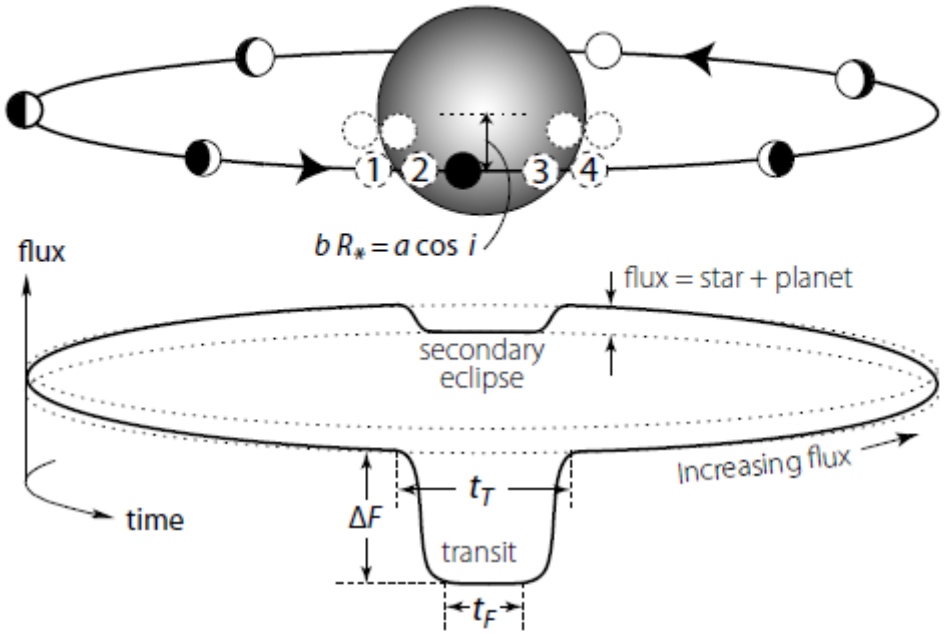

Figure 6.9: Schematic of a transit. During the transit, the planet blocks a fraction of the star light. After the transit, the planet's brighter day-side progressively comes into view, and the total flux rises. It drops again during the secondary eclipse as the planet passes behind the star. Dashed circles show the first to fourth contact points; those for smaller impact parameter (dotted) are more closely separated in time, and the ingress/egress slopes correspondingly steeper. The total transit duration t_T is between first and fourth contact, while t_F is timed between second and third contact. After Winn (2009, Figure 1).

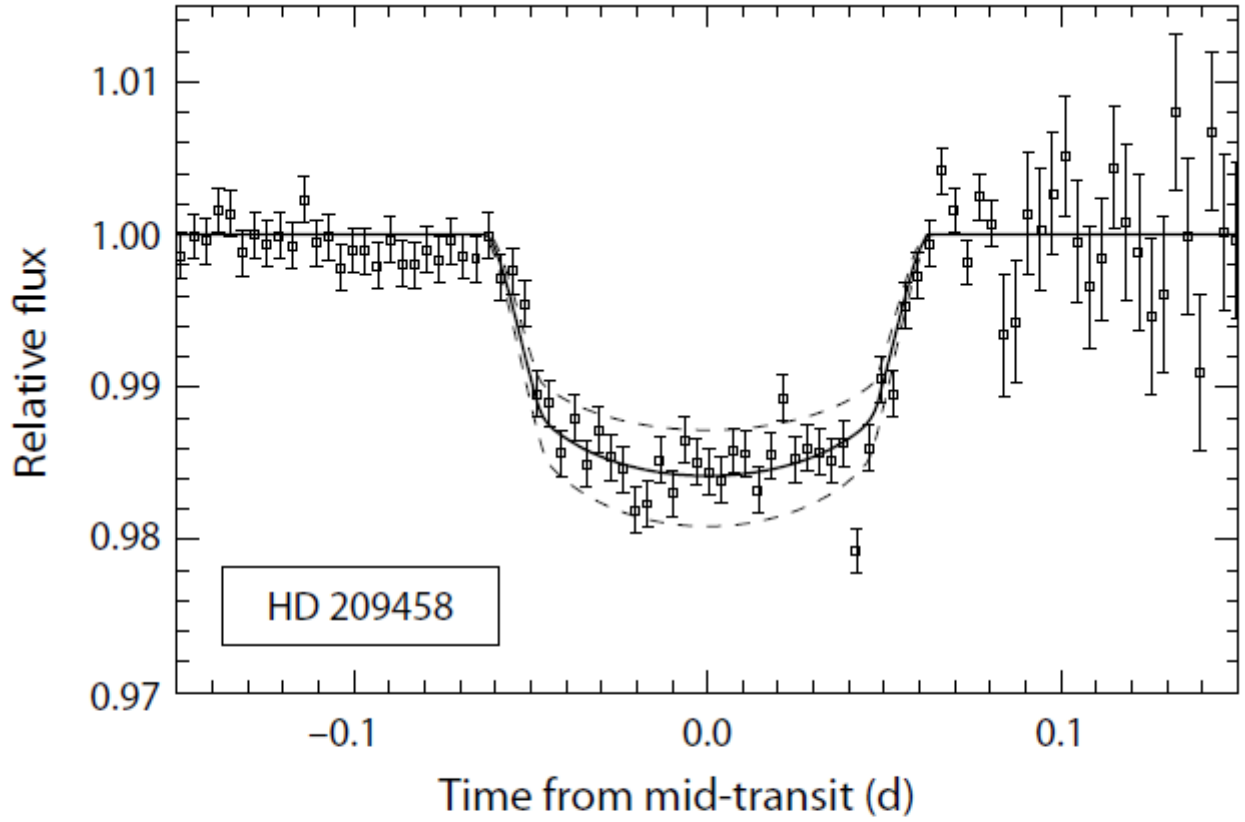

Figure 6.1: The first detected transiting exoplanet, HD 209458, showing the measured flux versus time. Measurement noise increases to the right due to increasing atmospheric air mass. From Charbonneau et al. (2000, Figure 2), reproduced by permission of the AAS.

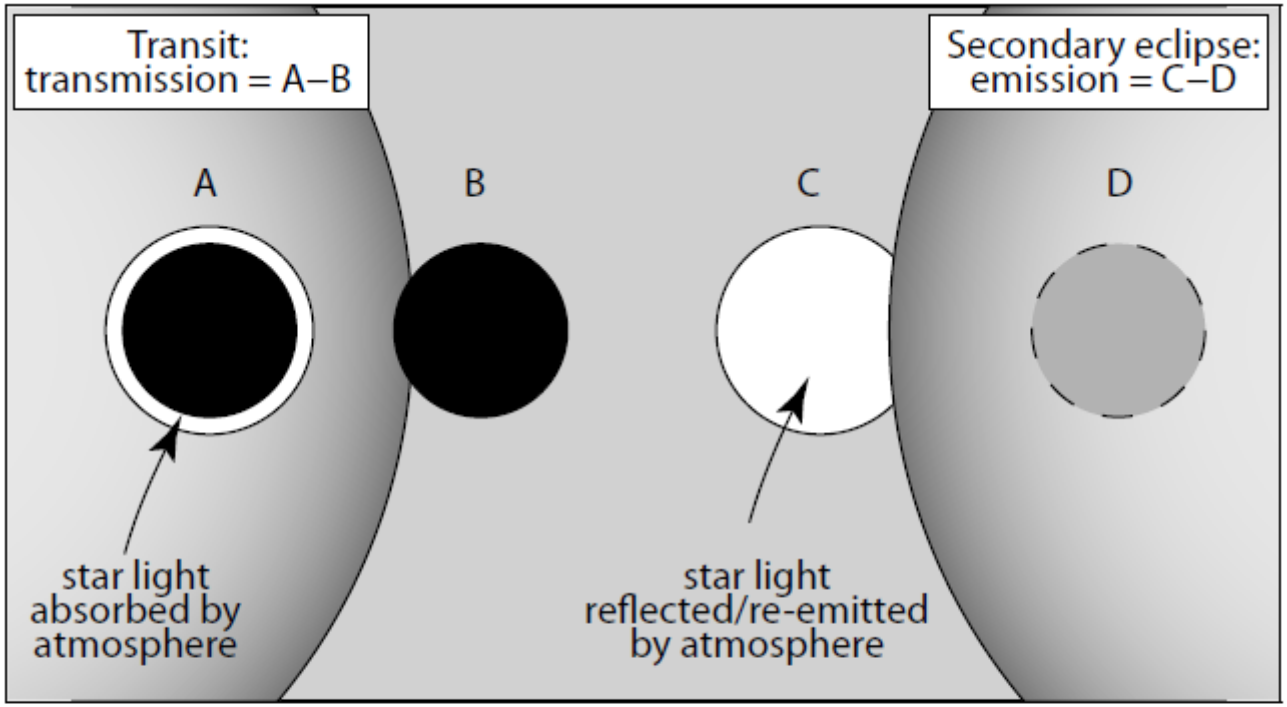

Figure 6.24: Geometry of transmission (left) and emission spectroscopy (right). During the transit, part of the background star light passes through the (annular) atmosphere of the planet. During the secondary eclipse, there is a switching off of the light reflected or emitted from the day-side surface of the planet.

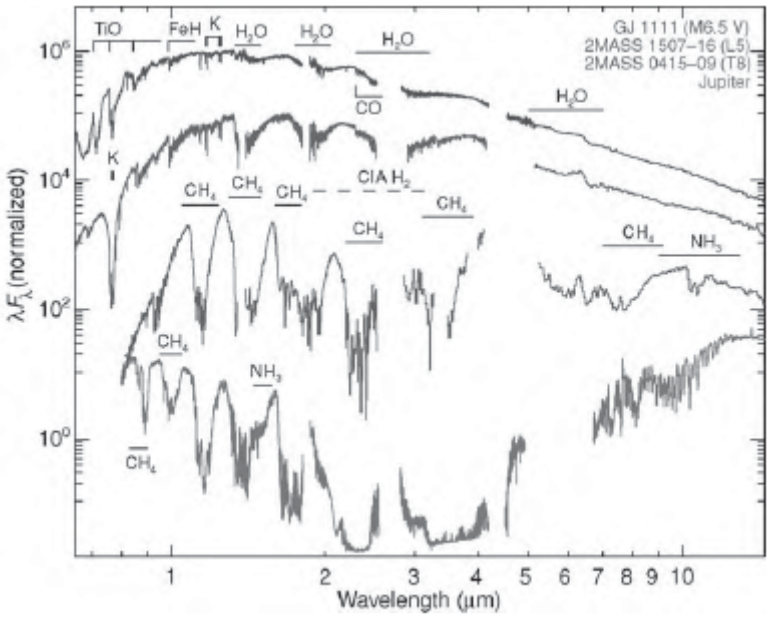

Figure 14.6 The observed spectra of four objects, from hot to cold (*top* to *bottom*): an M dwarf star, brown dwarfs with two different types of spectra (L and T) and Jupiter. Comparison of these spectra illustrates the changes in atmospheric chemistry and spectra that are seen as low-mass hydrogen–helium dominated objects (e.g., giant planets) cool over time. Water and refractory diatomic species dominate the M dwarf spectrum. In L and T dwarfs, the water absorption bands get progressively deeper, methane appears, and the refractory gasses disappear as they condense into solid grains. At still cooler temperatures, ammonia appears, and all water is condensed into clouds at Jupiter. The effective temperatures are about 2900 K in the M dwarf, 1600 K in the L5 brown dwarf, 700 K in the T8 brown dwarf and 130 K for Jupiter. Jupiter's spectrum shortwards of 3.5 μm is entirely reflected sunlight. (Courtesy Mark Marley and Mike Cushing)

Table 14.1 **Kepler-11's Planetary System**

	Period (d)	a (AU)	e	i (°)	R_p ($R_\oplus$)	M_p ($M_\oplus$)	ρ (kg/m^3)	$\mathcal{F}$ ($\mathcal{F}_\odot$)
b	10.304	0.091	0.04	89.6	1.8	1.9	1720	125
c	13.024	0.107	0.03	89.6	2.9	2.9	660	92
d	22.685	0.155	0.004	89.7	3.1	7.3	1280	44
e	32.000	0.195	0.01	88.9	4.2	8.0	580	27
f	46.689	0.250	0.01	89.5	2.5	2.0	690	17
g	118.381	0.466	<0.15	89.9	3.3	<25	–	4.8

Source: Lissauer et al. 2013.

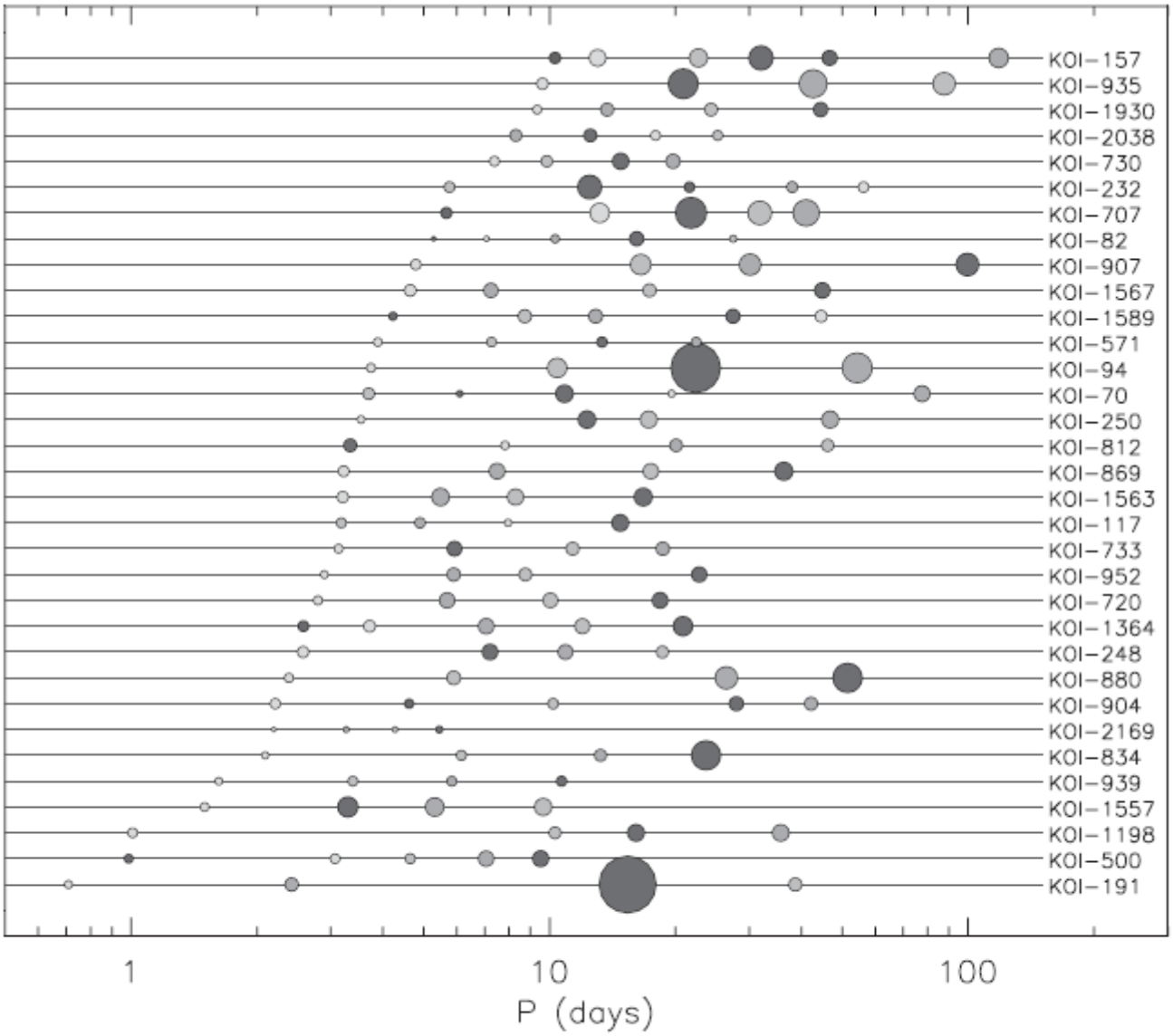

Figure 14.28 *Kepler* candidate planetary systems of four or more planets as of February 2012. Each *line* corresponds to one system, as labeled on the *right side* (the one dynamically unstable four-candidate planet system is not represented). Ordering is by the orbital period of the innermost planet. Planet radii are to scale relative to one another and are colored by decreasing size within each system: *red*, *orange*, *green*, *light blue*, *dark blue*, and *gray*. (Courtesy Daniel Fabrycky)

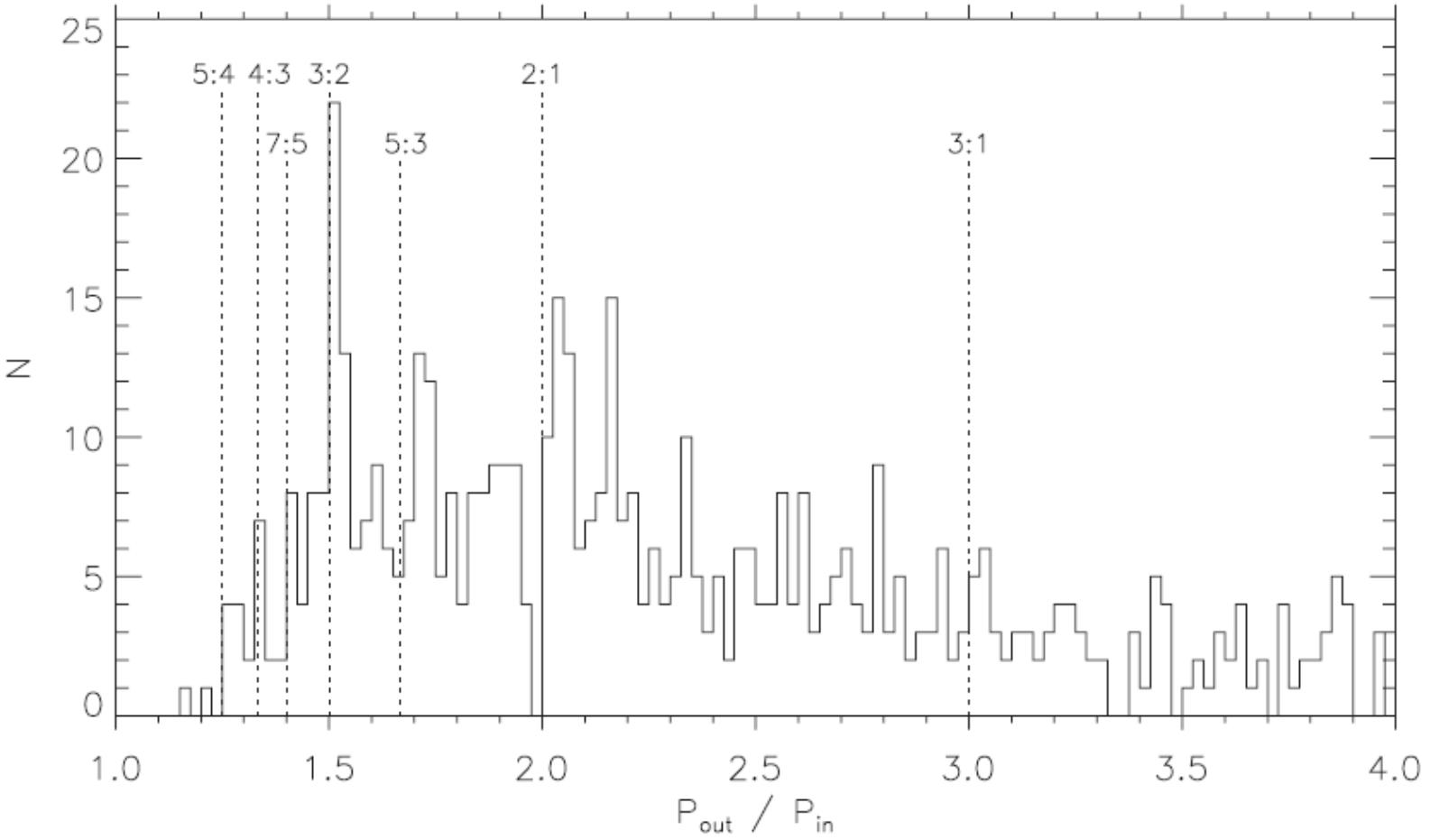

Figure 14.29 Histogram of period ratios for all pairs of planets (excluding the two dynamically unstable candidate pairs) within multiple planet systems observed by *Kepler* as of February 2012, out to a period ratio of 4. First-order (period ratios given in *top row*) and second-order (period ratios given in *second row*) resonances are marked by *dashed lines*. (Courtesy Daniel Fabrycky)

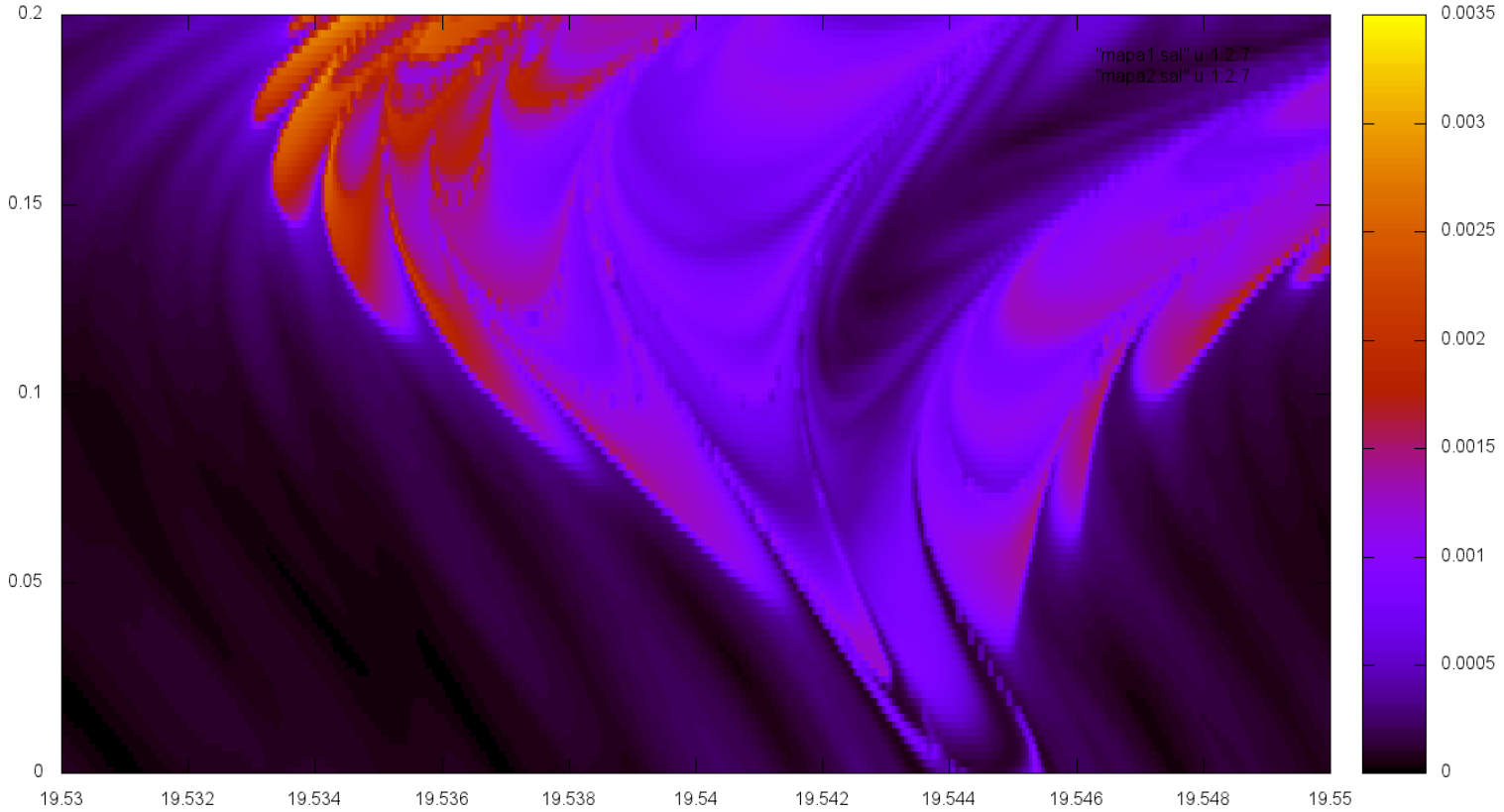
"mapa1.sal" u 1:2:7
"mapa2.sal" u 1:2:7
0.2
0.15
0.1
0.05
0
19.53
19.532
19.534
19.536
19.538
19.54
19.542
19.544
19.546
19.548
19.55
0.0035
0.003
0.0025
0.002
0.0015
0.001
0.0005
0

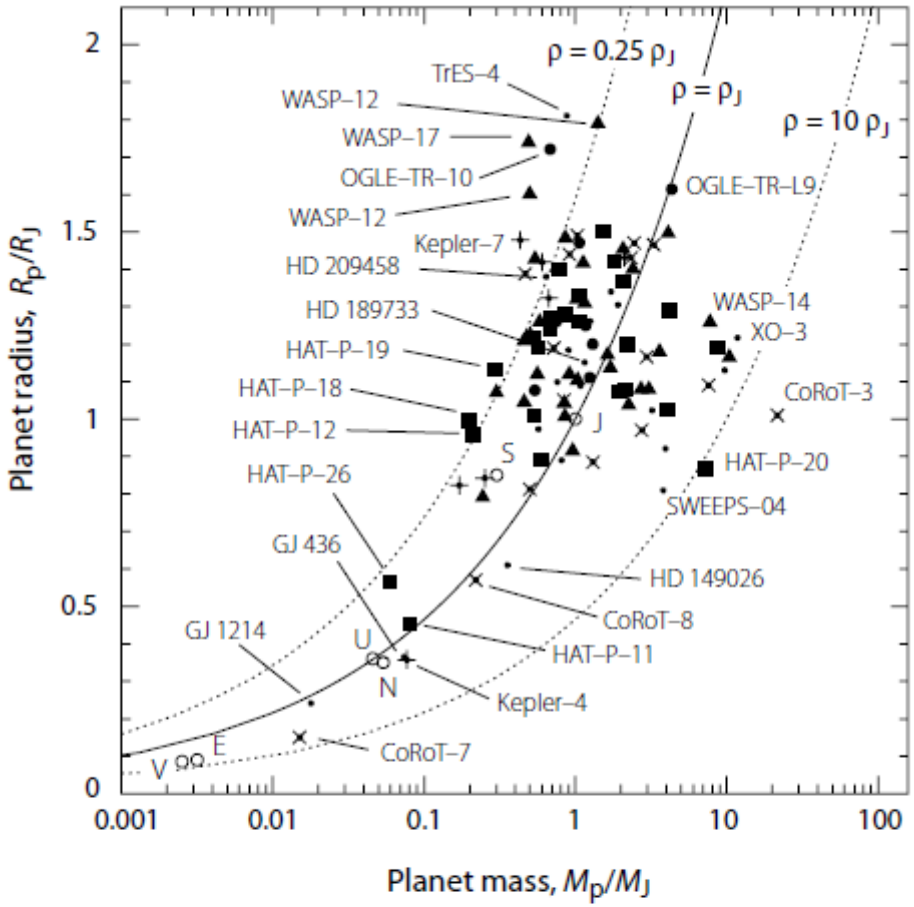

Figure 6.33: Mass–radius diagram for transiting exoplanets (● OGLE, ▲ WASP, ■ HAT, × CoRoT, + Kepler, · other). Data are from `exoplanet.eu`*, 2010 November 1 (Appendix D).* V, E, J, S, U, N *indicate positions of Venus, Earth, Jupiter, Saturn, Uranus, Neptune. Dashed lines are of constant density in Jovian units* $(0.25, 1, 10\rho_J)$*. CoRoT–3 b* $(22 M_J)$ *is a brown dwarf.*

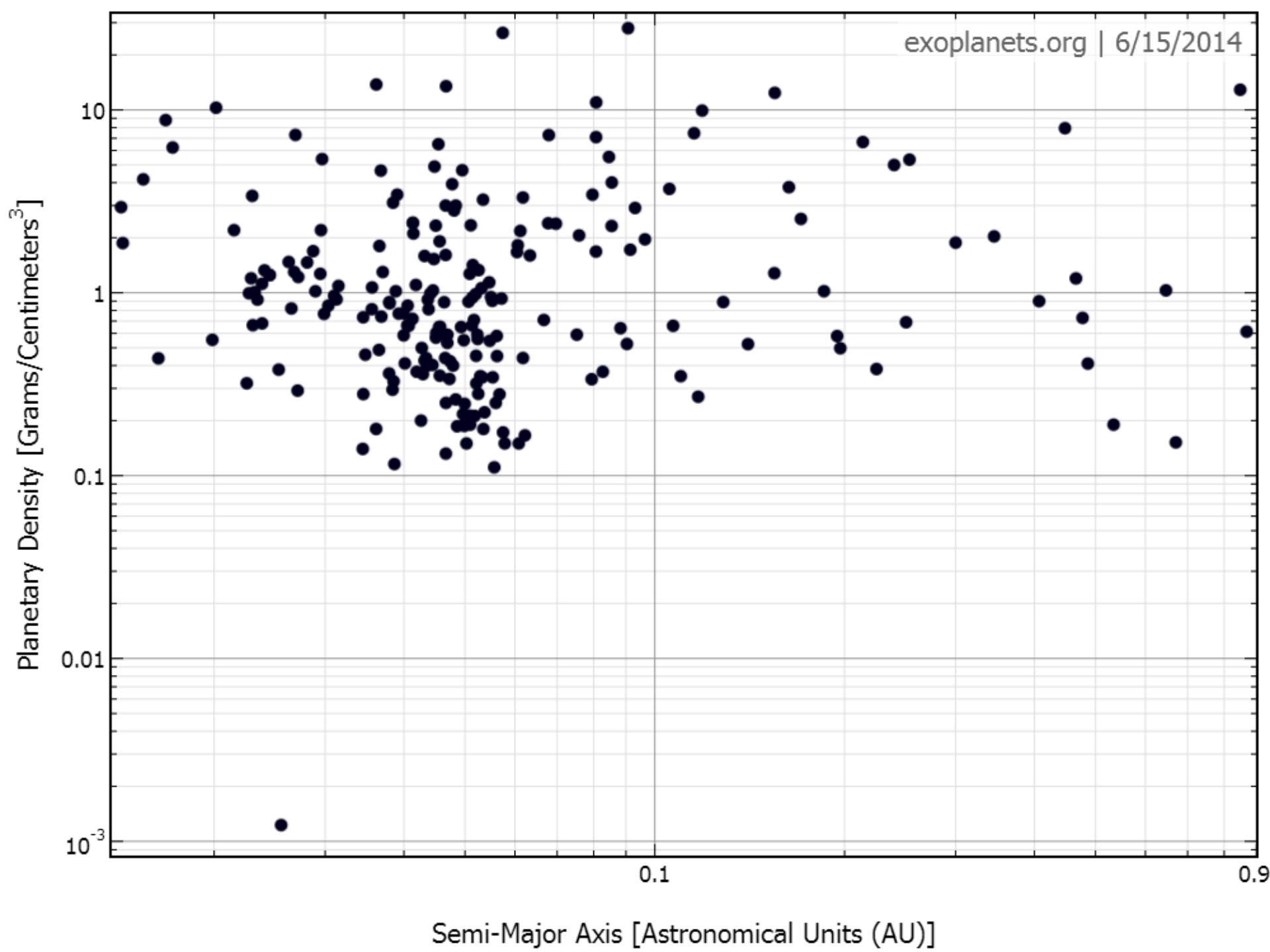
exoplanets.org | 6/15/2014
Planetary Density [Grams/Centimeters^3]
10
1
0.1
0.01
10^{-3}
0.1
0.9
Semi-Major Axis [Astronomical Units (AU)]

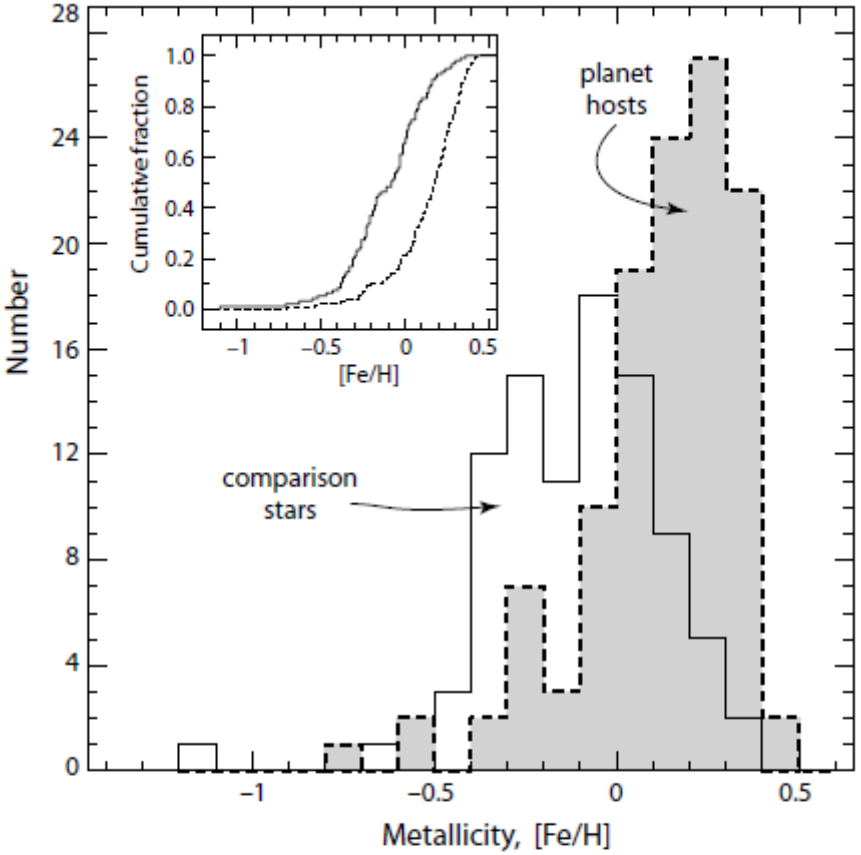

Figure 8.7: Metallicity distribution for 119 planet-host stars (shown as the dashed line, shaded), and for a volume-limited comparison sample of 94 stars with no known planets (continuous line, unshaded). The average metallicity difference of the two samples is 0.24 dex. Inset: cumulative distribution functions. A statistical Kolmogorov–Smirnov test shows that the probability that both distributions belong to the same population is $\sim 10^{-12}$. *From Santos et al. (2005, Figure 1), reproduced with permission © ESO.*

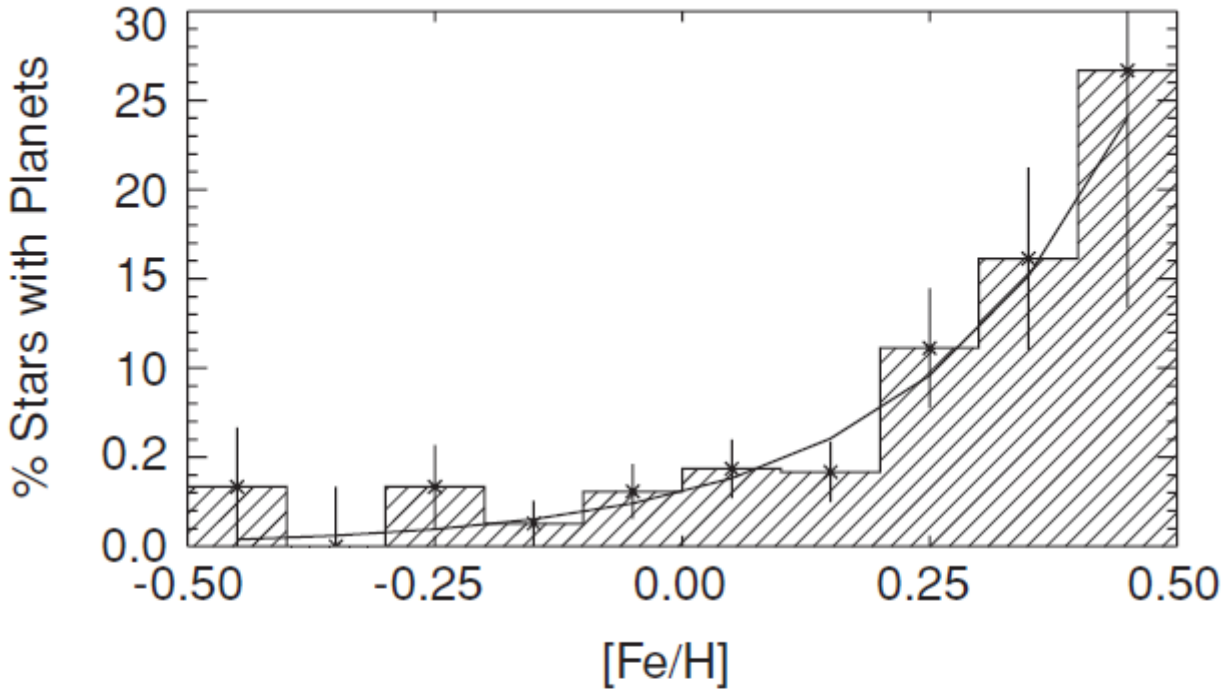

Figure 14.25 The fraction of Sun-like stars possessing giant planets with orbital periods of less than four years is shown as a function of stellar metallicity. Metallicity is measured on a logarithmic scale, with [Fe/H] = 0 corresponding to the solar value. (Fischer and Valenti 2005)

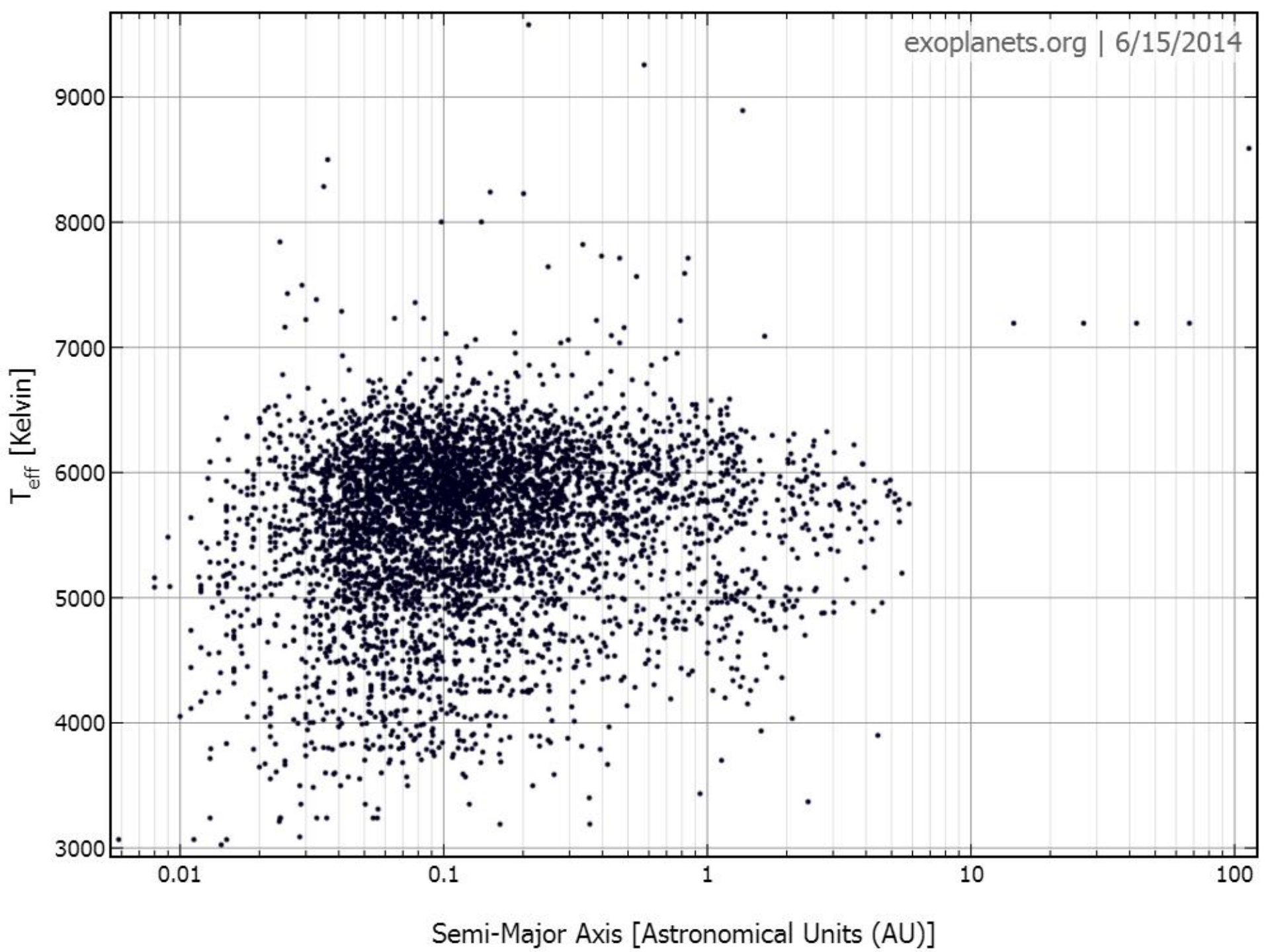
exoplanets.org | 6/15/2014
9000
8000
7000
6000
5000
4000
3000
T_{eff} [Kelvin]
0.01
0.1
1
10
100
Semi-Major Axis [Astronomical Units (AU)]

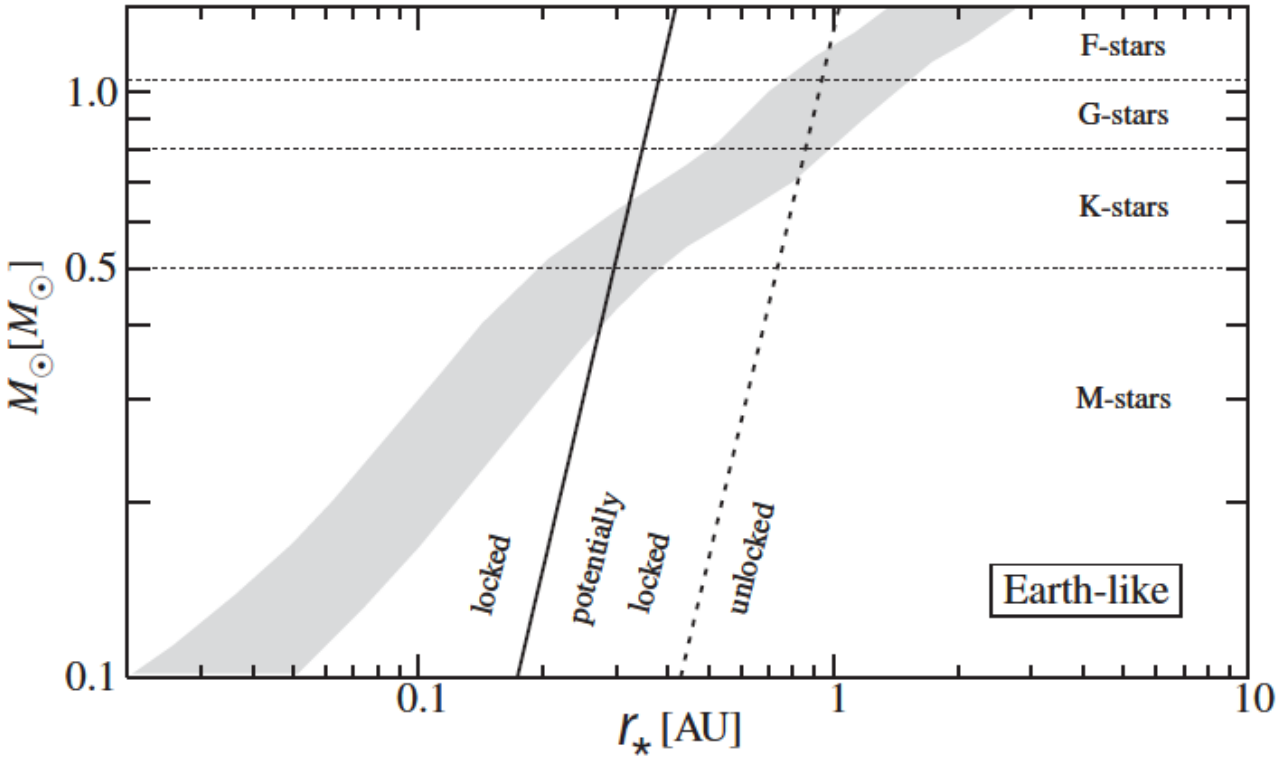

Figure 16.4 The *shaded region* represents the location of the circumstellar habitable zone (for Earth-like planets) as a function of stellar mass for zero-age main sequence stars. A rocky planet to the left of the *solid line* would have its rotation tidally locked in a (geologically) short period of time (§2.7.2) and henceforth always present the same hemisphere to its star, a planet to the right of the *dashed line* would likely not be in such a rotation state, but planets located between these two lines might or might not be in synchronous rotation. (Grießmeier et al. 2009)

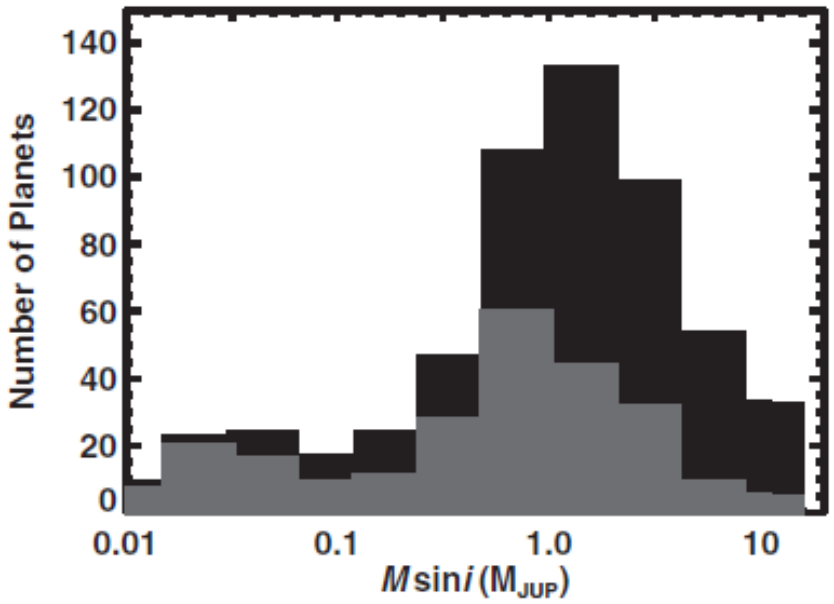

Figure 14.23 Histogram of the number of planets observed as a function of minimum planet mass, $M_p \sin i$, obtained from the same data set used to produce Figure 14.22. Each bin encompasses a factor of 2 in minimum mass. The *gray region* at the bottom represents planets with orbital periods of less than 30 days, and the *black region* shows the number of planets with longer periods. Because more massive planets are easier to detect, the tail-off in the distribution above 1–2 $M_{\oplus}$ is real, but the drop-off at smaller masses is a consequence of observational selection effects. Likewise, the shift in the distribution to smaller masses at shorter periods results from the larger radial velocity perturbations by planets orbiting closer to the star (eq. 14.1) and the greater number of orbits that these planets have covered since the highest precision radial velocity surveys have been underway. (Courtesy Geoff Marcy)

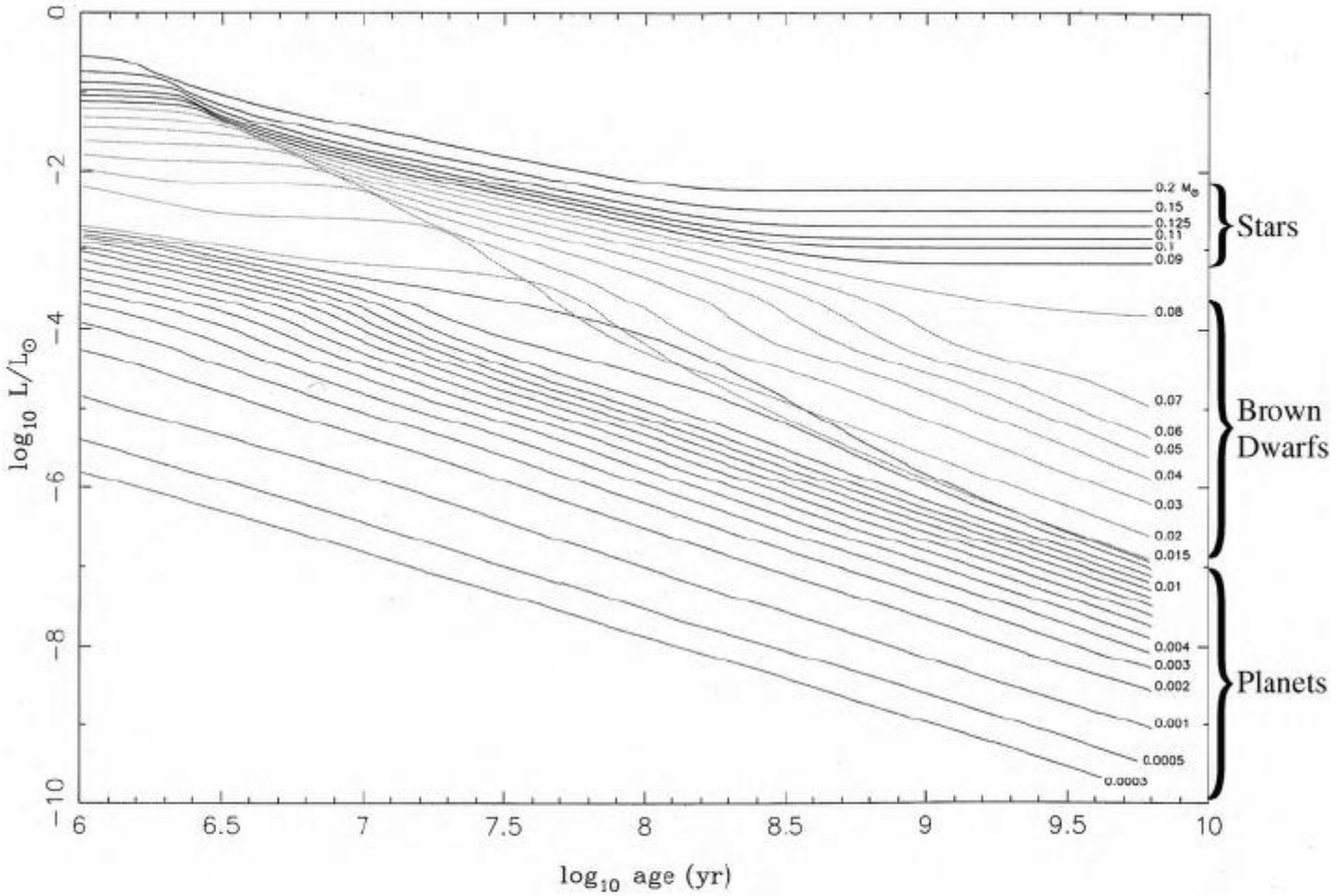

Figure 3.7 Evolution of the luminosity (in $\mathcal{L}_\odot$) of initially hot and distended very low mass stars and substellar objects plotted as functions of time (in years) after formation. All of these objects are isolated and have solar-metallicity. The stars, brown dwarfs and planets are shown as the upper, middle and lower sets of curves, respectively. The curves are labeled by the object's mass in units of $M_\odot$; the lowest curve corresponds to the mass of Saturn. All of the substellar objects become less luminous as they radiate away the energy released by their gravitational contraction from large objects to much more compact bodies with sizes of order $R_\clubsuit$. Stars ultimately level off in luminosity when they reach the hydrogen burning main sequence. In contrast, the luminosities of brown dwarfs and planets decline indefinitely. Objects with $M \gtrsim 0.012\ M_\odot$ exhibit plateaus between 10^6 and 10^8 years as a result of deuterium burning. The luminosities of the younger objects, especially giant planets $\lesssim 10^8$ years old, may be substantially smaller than the values shown here if they radiate away substantial portions of their accretion energy while they are growing. (Burrows et al. 1997)

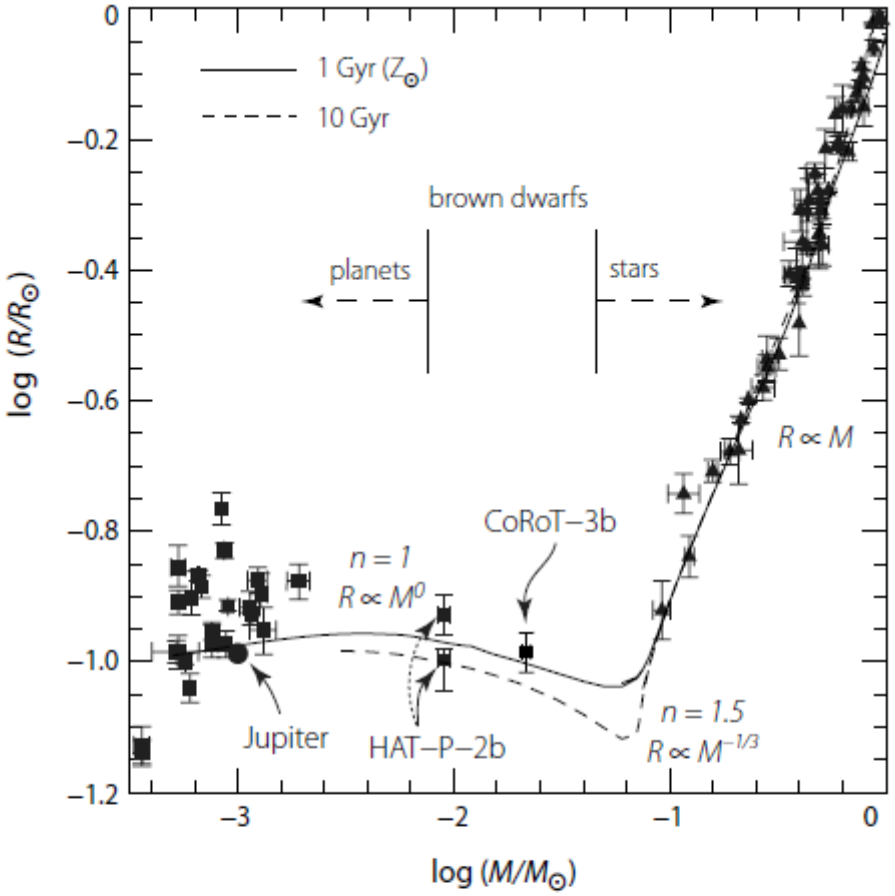

Figure 6.34: Mass–radius relation for stars and planets. Solid and short-dashed lines are models with solar composition for two isochrones, and n indicates the relevant polytropic index. Lines demarcating planets and stars are somewhat arbitrary. The CoRoT–3 b radius is from Deleuil et al. (2008). For HAT–P–2 b, both the original determination (lower point, Bakos et al., 2007a) and a later revision (upper point, Pál et al., 2010) are shown. From Chabrier et al. (2009, Figure 2).

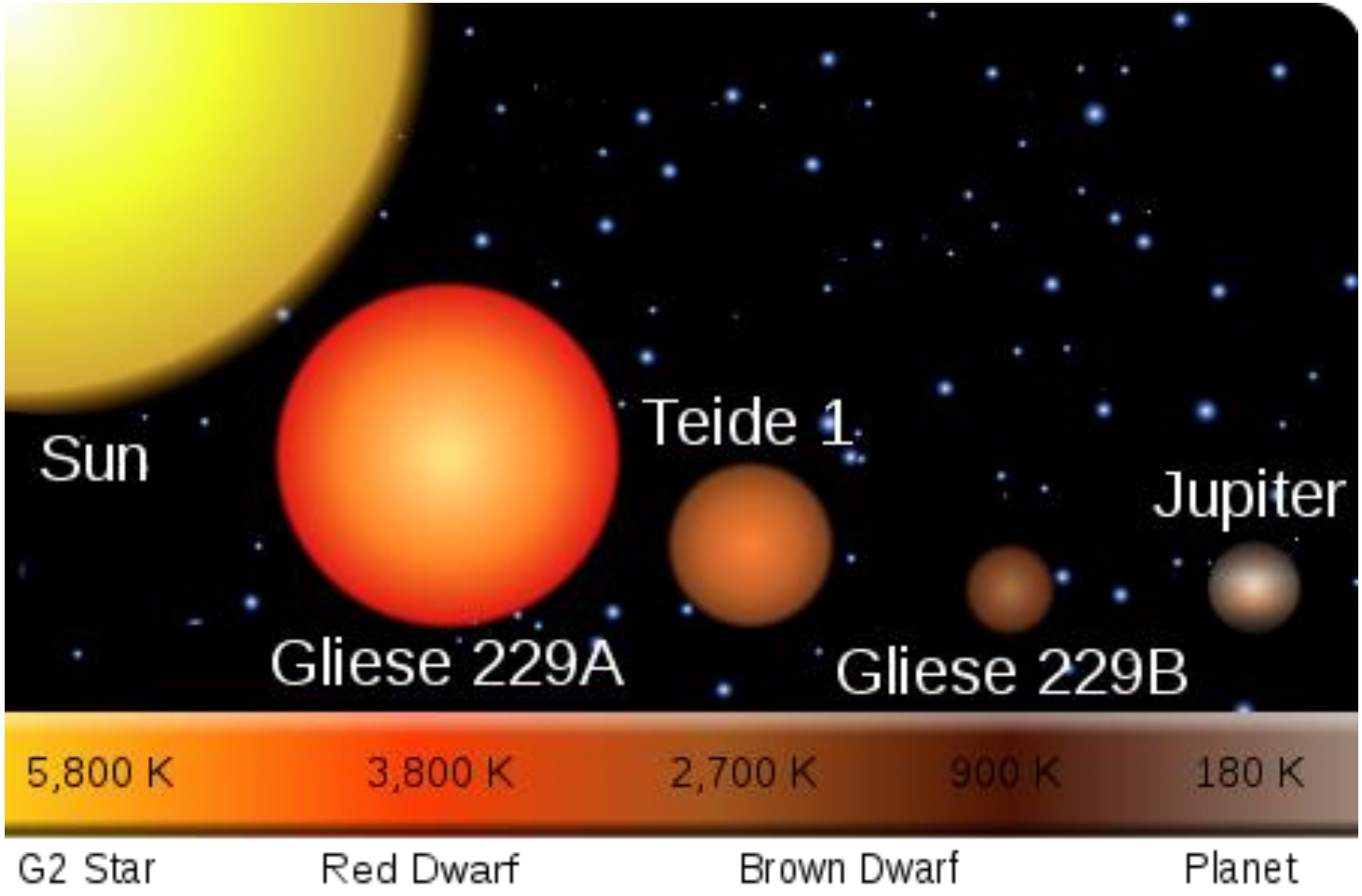
Sun
Gliese 229A
Teide 1
Gliese 229B
Jupiter
5,800 K
3,800 K
2,700 K
900 K
180 K
G2 Star
Red Dwarf
Brown Dwarf
Planet

Tabare Gallardo, Dpto. Astronomia, Facultad de Ciencias

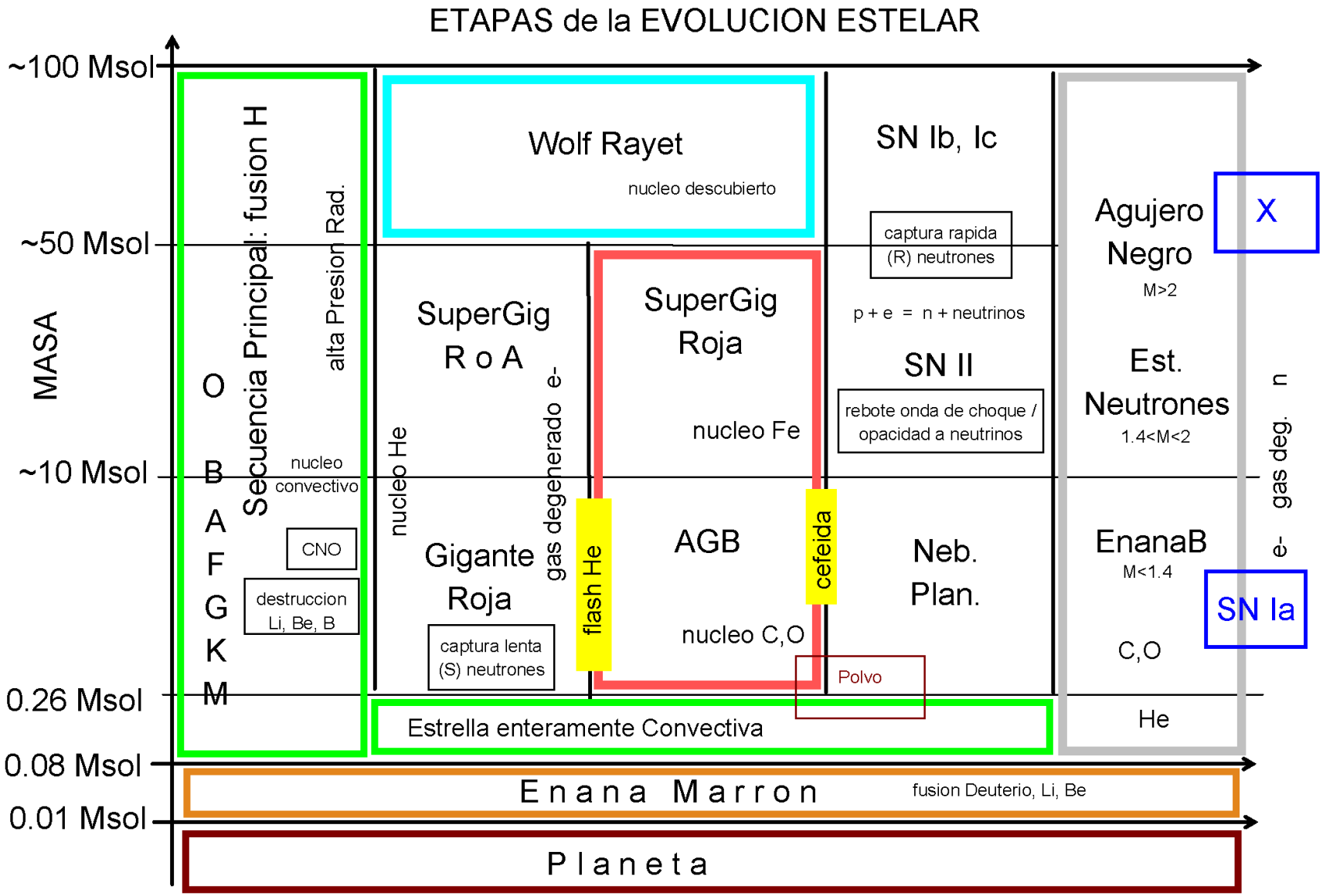

BIBLIOGRAFIA:

- The Exoplanet Handbook, Perryman
- Fundamental Planetary Science, Lissauer y de Pater
- exoplanets.org